Year: 2018

ATR-Mediated Global Fork Slowing and Reversal Assist Fork Traverse and Prevent Chromosomal Breakage at DNA Interstrand Cross-Links

Mutreja, Karun; Krietsch, Jana; Hess, Jeannine; Ursich, Sebastian; Berti, Matteo; Roessler, Fabienne K; Zellweger, Ralph; Patra, Malay; Gasser, Gilles; Lopes, Massimo

Abstract: Interstrand cross-links (ICLs) are toxic DNA lesions interfering with DNA metabolism that are induced by widely used anticancer drugs. They have long been considered absolute roadblocks for replication forks, implicating complex DNA repair processes at stalled or converging replication forks. Recent evidence challenged this view, proposing that single forks traverse ICLs by yet elusive mechanisms. Combining ICL immunolabeling and single-molecule approaches in human cells, we now show that ICL induction leads to global replication fork slowing, involving forks not directly challenged by ICLs. Active fork slowing is linked to rapid recruitment of RAD51 to replicating chromatin and to RAD51/ZRANB3-mediated fork reversal. This global modulation of fork speed and architecture requires ATR activation, promotes single-fork ICL traverse-here, directly visualized by electron microscopy-and prevents chromosomal breakage by untimely ICL processing. We propose that global fork slowing by remodeling provides more time for template repair and promotes bypass of residual lesions, limiting fork-associated processing.

Cell Reports

ATR-Mediated Global Fork Slowing and Reversal Assist Fork Traverse and Prevent Chromosomal Breakage at DNA Interstrand Cross-Links

Graphical Abstract
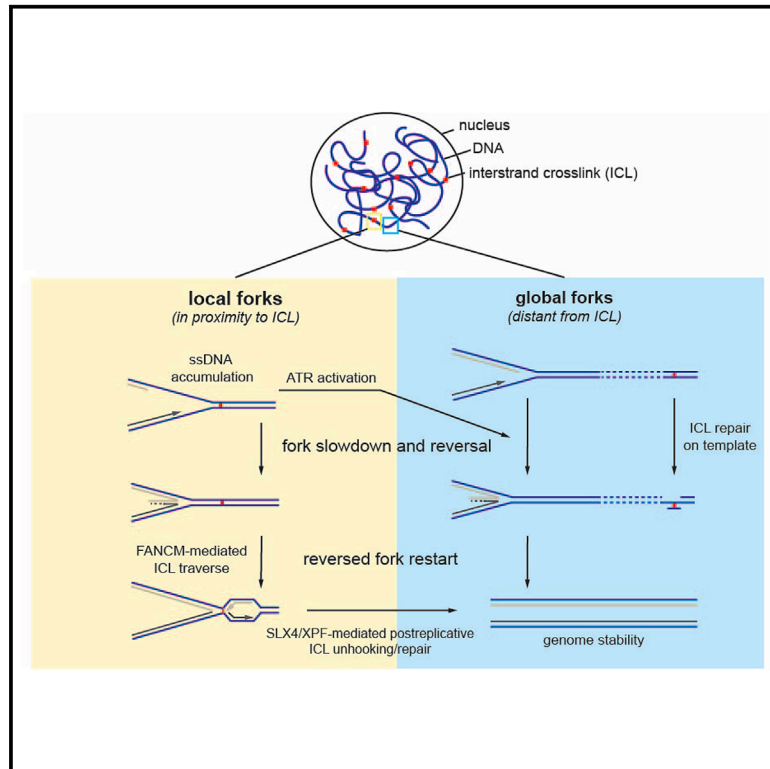
Authors

Karun Mutreja, Jana Krietsch,
Jeannine Hess, ..., Malay Patra,
Gilles Gasser, Massimo Lopes

Correspondence

lopes@imcr.uzh.ch

In Brief

Replication-coupled repair of DNA interstrand cross-links (ICLs) promotes resistance to chemotherapeutic treatments. Visualizing individual lesions and replication intermediates, Mutreja et al. report that forks slow down and reverse both at ICLs and away from lesions. This ATR-mediated response assists lesion bypass during replication and limits chromosomal breakage by fork-associated processing.

Highlights

- Fork slowing and reversal are also observed at forks not directly challenged by ICLs

- Fork reversal assists ICL traverse and limits DSBs associated with ICL unhooking

- ICL traverse can be directly visualized in human cells by electron microscopy

- ATR mediates global fork slowing and reversal upon different genotoxic treatments

CellPress

ATR-Mediated Global Fork Slowing and Reversal Assist Fork Traverse and Prevent Chromosomal Breakage at DNA Interstrand Cross-Links

Karun Mutreja,[1] Jana Krietsch,[1] Jeannine Hess,[3,4] Sebastian Ursich,[1] Matteo Berti,[1] Fabienne K. Roessler,[1,2]
Ralph Zellweger,[1] Malay Patra,[3] Gilles Gasser,[3,5] and Massimo Lopes[1,6,*]
[1]Institute of Molecular Cancer Research, University of Zurich, Winterthurerstrasse 190, CH-8057 Zurich, Switzerland
[2]Center for Microscopy and Image Analysis, University of Zurich, Winterthurerstrasse 190, CH-8057 Zurich, Switzerland
[3]Department of Chemistry, University of Zurich, Winterthurerstrasse 190, CH-8057 Zurich, Switzerland
[4]Present address: Department of Chemistry, University of Cambridge, Lensfield Road, Cambridge CB2 1EW, United Kingdom
[5]Present address: Chimie ParisTech, PSL University, Laboratory for Inorganic Chemical Biology, F-75005 Paris, France
[6]Lead Contact
*Correspondence: lopes@imcr.uzh.ch
 https://doi.org/10.1016/j.celrep.2018.08.019

SUMMARY

Interstrand cross-links (ICLs) are toxic DNA lesions interfering with DNA metabolism that are induced by widely used anticancer drugs. They have long been considered absolute roadblocks for replication forks, implicating complex DNA repair processes at stalled or converging replication forks. Recent evidence challenged this view, proposing that single forks traverse ICLs by yet elusive mechanisms. Combining ICL immunolabeling and single-molecule approaches in human cells, we now show that ICL induction leads to global replication fork slowing, involving forks not directly challenged by ICLs. Active fork slowing is linked to rapid recruitment of RAD51 to replicating chromatin and to RAD51/ ZRANB3-mediated fork reversal. This global modulation of fork speed and architecture requires ATR activation, promotes single-fork ICL traverse—here, directly visualized by electron microscopy—and prevents chromosomal breakage by untimely ICL processing. We propose that global fork slowing by remodeling provides more time for template repair and promotes bypass of residual lesions, limiting fork-associated processing.

INTRODUCTION

Interstrand cross-links (ICLs) are DNA lesions that prevent DNA strand separation, thereby interfering with crucial DNA transactions for cellular proliferation, such as replication and transcription. In light of this toxicity, ICL-inducing agents, such as cisplatin and nitrogen mustards, are among the most widely used compounds in cancer treatment (Deans and West, 2011). Moreover, ICL can be endogenously induced by reactive aldehyde species arising as by-product of natural cellular metabolism (Langevin et al., 2011). Repair of these lesions has been

thoroughly studied in recent years and may occur in a replication-dependent or -independent manner (Williams et al., 2013). Several DNA repair pathways have been implicated in ICL replication and repair. These mechanisms have received major attention since the discovery that the human bone marrow failure syndrome Fanconi anemia (FA), also associated with cancer predisposition, results from mutations in more than 20 independent genes that play a common crucial role in ICL repair (Kottemann and Smogorzewska, 2013). These include factors required to incise the DNA backbone for ICL unhooking—such as SLX4 and XPF/ERCC1 (Klein Douwel et al., 2014)—homologous recombination (HR) factors to repair associated double-stranded breaks (DSBs)—such as RAD51, BRCA1/BRIP1, BRCA2, and PALB2—and translesion polymerases to synthesize DNA opposite the unhooked ICL (Zhang and Walter, 2014). Many other FA factors regulate this pathway by associating in the so-called FA "core-complex," which mediates ubiquitination of FANCD2 and FANCI, a crucial regulatory event in ICL replication and repair (Ceccaldi et al., 2016).

ICLs have long been seen as absolute roadblock for the replication forks; thus, most ICL repair transactions described above have been suggested to occur at stalled forks (Zhang and Walter, 2014). Mechanisms and kinetics of these events have been studied in great detail in cell-free *Xenopus* egg extracts, using plasmids carrying a single synthetic ICL (Räschle et al., 2008). These studies have supported a model in which a first fork is stalled at the ICL, but ICL processing and removal require a second incoming fork and replisome disassembly (Long et al., 2014; Zhang et al., 2015). An important implication of these studies is that ICL unhooking, DSB formation, and HR-mediated repair occur relatively late, once bulk DNA replication has been achieved (Long et al., 2011). Recent studies in mammalian cells have, however, challenged this model. A key ICL-repair factor FANCD2 has been shown to associate with the replisome, regulating unwinding by the replicative helicase (Lossaint et al., 2013). Furthermore, key ubiquitin-regulated events that mediate resistance to ICL-inducing agents—i.e., FANCD2 ubiquitination and recruitment of FAN1 nuclease—are not required for ICL repair, but rather to regulate replication fork progression

(Lachaud et al., 2016), suggesting that active regulation of DNA synthesis may play a pivotal—albeit undefined—role in the response to ICL-inducing agents. Moreover, single-molecule studies in mammalian cells have surprisingly shown that—despite some pausing—single forks can efficiently traverse ICLs (Huang et al., 2013), challenging the fork convergence model. ICL traverse was shown to depend on FANCM, a DNA translocase that mediates replication fork remodeling *in vitro* (Gari et al., 2008; Huang et al., 2013). However, mechanistic understanding of how template unwinding and fork restart are achieved after fork stalling at ICLs is still very limited. ICL traverse would in principle require *de novo* template unwinding beyond the lesion—which challenges established dogmas of helicase recruitment and regulation—and may require extensive remodeling of fork architecture and/or changes in replisome composition or function.

Recent direct visualization of replication fork architecture in human cells has uncovered extensive remodeling of forks into four-way junctions—a process known as replication fork reversal—in response to different conditions of replication stress (Berti and Vindigni, 2016; Neelsen and Lopes, 2015; Quinet et al., 2017). Fork reversal was shown to prevent chromosomal breakage upon different treatments and has emerged as a reversible, genetically controlled transaction supporting genome stability upon genotoxic treatments (Berti et al., 2013; Ray Chaudhuri et al., 2012; Thangavel et al., 2015). The key recombinase RAD51 as well as the DNA translocase ZRANB3 were shown to drive replication fork reversal *in vivo*, thereby modulating the rate of fork progression and error-free DNA damage tolerance in human cells (Vujanovic et al., 2017; Zellweger et al., 2015). Surprisingly, fork remodeling was found to be largely independent from the type and the dose of the genotoxic treatment (Zellweger et al., 2015), suggesting that it may represent a general cellular response, promoted and limited by specific signaling mechanisms.

Ataxia telangiectasia and Rad3-related (ATR) is the apical kinase coordinating replication stress responses in human cells (Saldivar et al., 2017). ATR and its key target CHK1 limit origin firing during unperturbed S phase (Katsuno et al., 2009) and upon replication stress (Costanzo et al., 2003; Karnani and Dutta, 2011), limiting exhaustion of nucleotides and of the single-strand binding protein RPA, thereby preventing replication catastrophe (Toledo et al., 2013). In both yeast and human cells, ATR modulates origin firing by limiting chromatin recruitment of the initiation factor CDC45, which along with activation of the DDK (CDC7) is essential to fire replication origins. ATR inhibits CDC45 loading via phosphorylation of the replisome component Sld3/Treslin and of the histone methyltransferase MLL (Guo et al., 2015; Liu et al., 2010; Lopez-Mosqueda et al., 2010; Zegerman and Diffley, 2010).

Although numerous replisome components, accessory factors, and HR proteins have been identified as ATR targets (Ahlskog et al., 2016; Errico and Costanzo, 2012; Lossaint et al., 2013; Murphy et al., 2014; Somyajit et al., 2013; Vassin et al., 2009), whether and how ATR modulates fork progression upon stress has been debated. Inactivation of ATR or CHK1 affects fork progression in unperturbed conditions, mostly as a consequence of deregulated origin firing (Petermann et al., 2006, 2010). Although CHK1 was suggested to actively slow down

replication upon topoisomerase inhibition (Seiler et al., 2007), assessing reliably whether ATR/CHK1 directly control fork speed upon genotoxic stress requires genetic uncoupling of their functions at origins and at active forks. The relevance of ATR signaling in fork remodeling is also unknown. Yeast studies displayed increased reversal of stalled forks upon inactivation of the replication checkpoint kinase Rad53 (Sogo et al., 2002). A negative role for ATR in fork reversal was also suggested in human cells, based on the inhibitory ATR-dependent phosphorylation of the fork remodeling enzyme SMARCAL1 (Couch et al., 2013). However, extensive electron microscopy (EM) analysis upon different treatments revealed no association between reversed fork frequency and CHK1 phosphorylation (Zellweger et al., 2015), leaving the question unresolved.

Here, we provide evidence that early RAD51 recruitment during ICL replication mediates rapid replication fork reversal upon ICL induction. Fork remodeling involves far more forks than those stalled at ICLs and mediates global fork slowing, which assists ICL traverse by single forks and prevents incision-dependent DSBs. ATR signaling mediates both fork reversal and global fork slowing in response to ICLs and other treatments. Overall, these data suggest that—besides inhibition of origin firing—ATR modulates fork speed globally to assist DNA damage bypass by ongoing forks, thereby promoting genome stability during replication.

RESULTS

RAD51 Recruitment during ICL Replication Precedes DSB Formation

To study replication stress associated with ICL-inducing treatments, we treated U2OS cells with trimethylpsoralen (TMP) combined with UVA treatment, which reportedly induces DNA lesions with a much higher ICL/monoadducts ratio than cisplatin or mitomycin C (Huang et al., 2013; Lai et al., 2008). We refined a previously published protocol for chemical synthesis of digoxygenin-tagged TMP (DIG-TMP) (Figure S1A; STAR Methods), which allows monitoring ICLs by a specific antibody in most approaches used in this study. We applied TMP and its tagged derivative to cultured U2OS cells and identified doses of (DIG-)TMP and UVA inducing—only when combined—delayed progression through S and G2 phases (Figure S1B). These treatments allow cell cycle resumption and survival of most cells (Figures S1C–S1E), similarly to mitomycin C (MMC) acute treatments previously used to study ICL repair (Figure S1F) (Tian et al., 2015). In these conditions, we observed rapid ICL formation (DIG detection), DNA damage response (DDR) activation (H2AX phosphorylation, γH2AX), and reduced EdU incorporation, dependent on the combination of (DIG-)TMP and UVA treatments (Figures 1A, S2A, and S2B). Furthermore, these combined treatments induced delayed progression of ongoing replication forks—detected by DNA fiber analysis—comparable to mild MMC treatments used in previous studies (Figure S2C) (Zellweger et al., 2015). As expected, recovery from ICL-induced DDR activation and cell cycle delay required FANCD2 (Figures S2D and S2E), a key ICL repair factor (Kottemann and Smogorzewska, 2013). Overall, these sublethal (DIG-)TMP/UVA treatments recapitulate all expected marks of
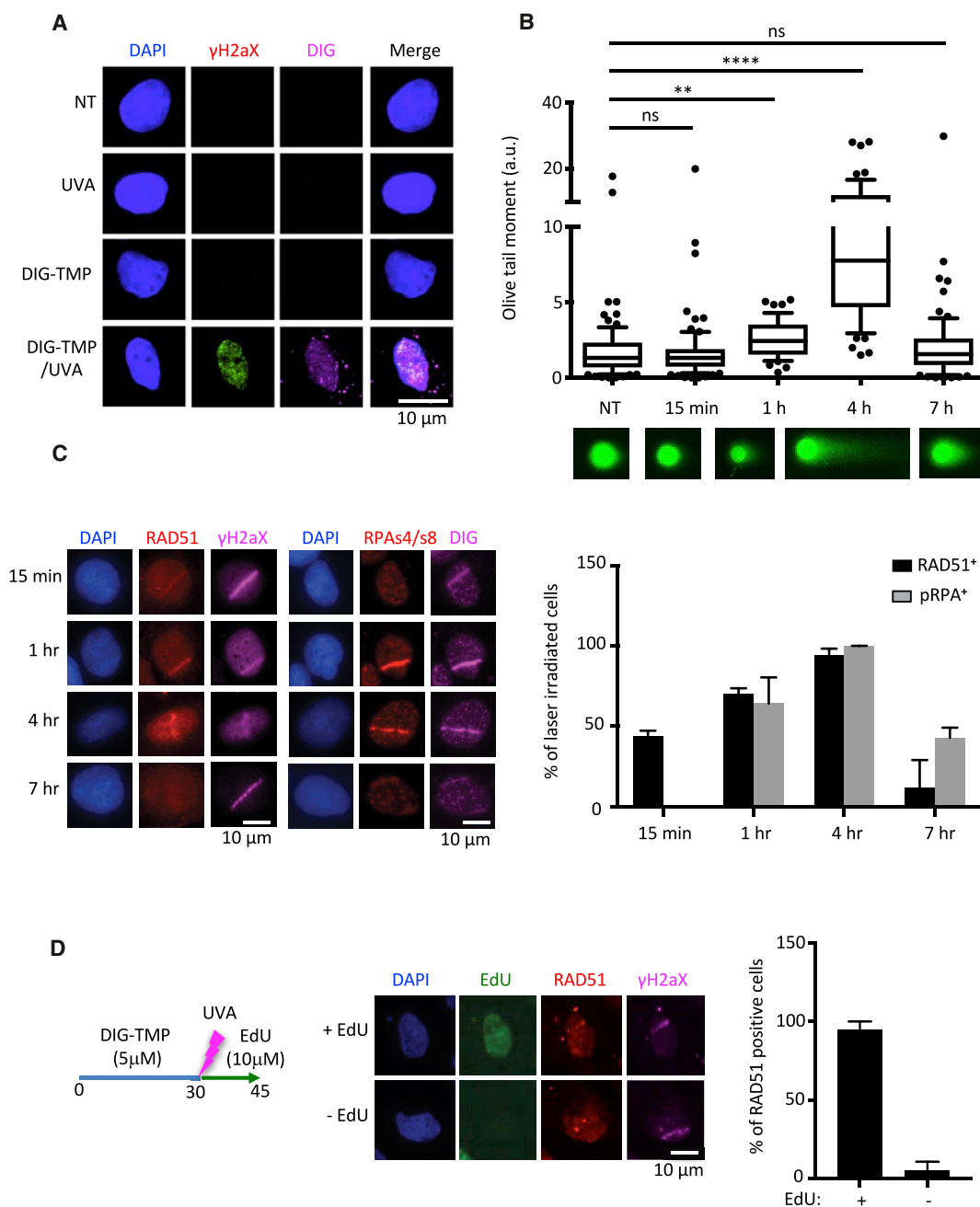
Figure 1. RAD51 Recruitment during ICL Replication Precedes DSB Formation

(A) Immunofluorescence (IF) analysis of γH2AX and DIG in U2OS cells 30 min after optional treatment with DIG-TMP (5 μM) and UVA (3 J/cm^2) alone, or in combination.

(B) Kinetics of DNA double-strand break (DSB) formation assessed by neutral comet assay after ICL induction by TMP (30 nM) and UVA (300 mJ/cm^2). Representative comets (bottom) and statistical analysis (top). At least 50 comets were scored per sample. Kruskal-Wallis test (****p < 0.0001; **p < 0.01; and ns, not significant).

(C) Kinetics of γH2AX, RAD51, pRPAs4/s8, and DIG at the site of UVA laser irradiation. Representative IF images (left) and percentage of laser-irradiated cells that were RAD51 or pRPA positive (right).

(D) Colocalization of RAD51 and gH2AX in EdU positive (+) and negative (−) cells. Cells were treated with DIG-TMP/UVA as in (A) followed by a 15-min EdU pulse. Experimental setup (left), representative images (middle), and percentage of RAD51-positive cells in EdU+/− cells (right). A minimum of 100 cells was analyzed per sample.

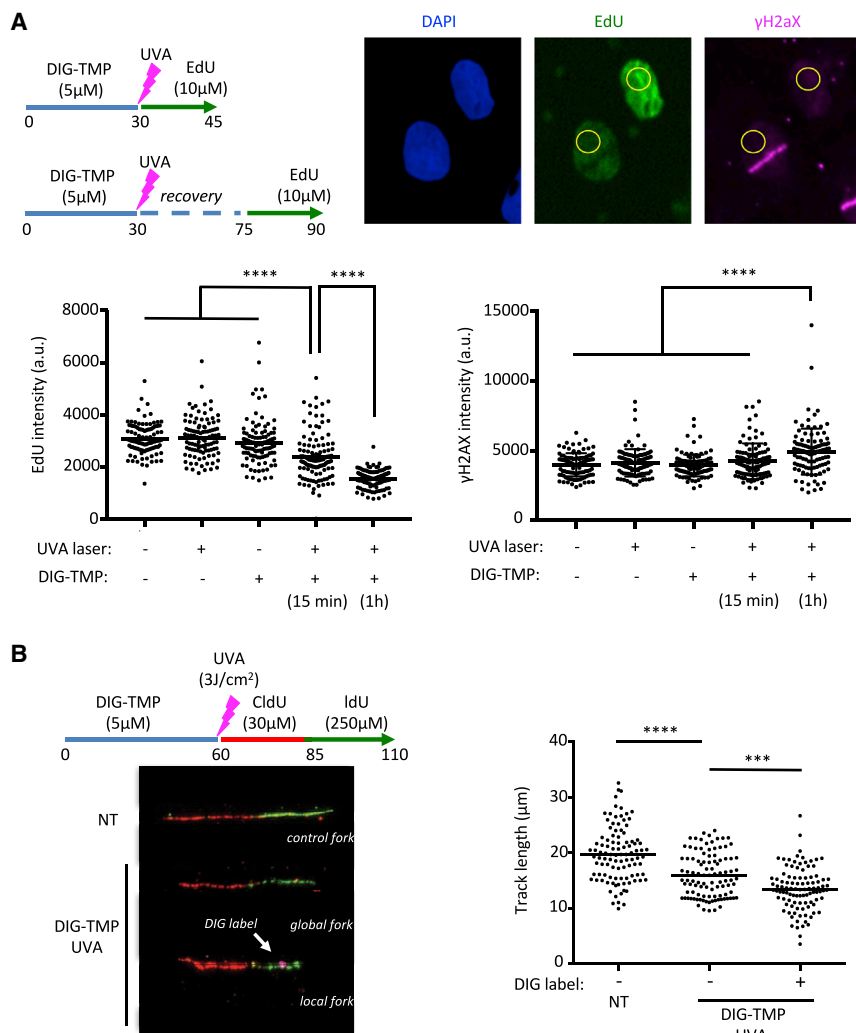(C and D) Error bars indicate SD. See also Figures S1 and S2.

A

DAPI EdU γH2aX

Figure 2. Induction of ICLs Reduces Fork Progression at Damaged, but Also at Undamaged Forks

(A) Assessment of DNA synthesis rate (EdU incorporation) and DNA damage signaling (γH2AX intensity) in regions of interest (ROIs) (yellow circle) outside the irradiated area. Experimental setup (top, left): U2OS cell were treated with DIG-TMP/UVA and pulsed with EdU—either immediately or after 45-min recovery. Representative images (top, right). Statistical analysis of EdU (bottom, left) or γH2AX (bottom, right) intensity in the ROIs. At least 100 cells were analyzed per sample. Kruskal-Wallis test (****p < 0.0001). Error bars indicate SD.

(B) Analysis of DNA fiber track length in the presence or absence of an ICL (indicated by the DIG label). Experimental setup (top, left). Representative images for DNA fiber categories (bottom, left). Total replication tract length (red plus green) was measured in U2OS cells treated as indicated for tracts without ICL (no DIG-label, global fork) and tracts containing an ICL (DIG-label, local fork). A minimum of 100 tracts was analyzed per sample. Kruskal-Wallis test (****p < 0.0001; ***p < 0.001). See also Figure S3.

B

(Long et al., 2011), reflects a specific function of the protein during DNA replication.

ICL Induction Reduces Fork Progression at Damaged and Undamaged Forks

We next took advantage of local induction and monitoring of ICLs (Figure S3A) to assess the global nuclear response to this treatment, in terms of DNA damage signaling (γH2AX) and DNA synthesis rate (EdU incorporation). As expected, γH2AX and a drastic reduction in EdU signals were both readily observed at UVA-laser stripes, reflecting direct replication impairment and DNA damage signaling during ICL replication (Figure 2A). However, we also observed a significant reduction of EdU incorporation on subnuclear compartments that were not exposed to UVA irradiation, as early as 15 min after irradiation. A parallel increase in γH2AX was observed in the same "undamaged" compartments and became statistically significant 1 hr after the local treatment (Figure 2A). A reduced rate of DNA synthesis may reflect the reported inhibition of new origin firing and/or active slowdown of ongoing forks. To directly assess a possible effect of ICL induction on the global progression of replication forks, we performed DNA fiber-spreading assays combined with direct detection of DIG-TMP lesions, thereby distinguishing ongoing replication forks that did (*local* forks) or did not (*global* forks) encounter an ICL during the labeling periods (Figures 2B and S3B). In our experimental conditions, *local* forks consistently represented ≈10% of the total ongoing forks scored in DIG-TMP/UVA-treated cells (Figure S3C) and expectedly showed a marked decrease in fork progression rate compared to ongoing forks in untreated cells

ICL-associated replication stress. Although the DNA lesions were readily detected within minutes, ICL-associated DSBs are detected by neutral comet assays only transiently and at later time points (1–4 hr after treatment; Figure 1B), supporting a model for ICL repair that invokes slow ICL processing by structure-specific nucleases and transient DSB formation (Zhang and Walter, 2014). ICLs and associated marks can also be induced in subnuclear compartments, by coupling DIG-TMP treatments with laser-administered UVA light (Figure S3A). As expected, RPA-s4/s8 phosphorylation—which requires breakage of the forks challenged by genotoxic stress (Zellweger et al., 2015)—follows the kinetics of direct DSB detection (Figures 1B and 1C). However, a significant fraction of DIG-TMP/UVA-treated cells displayed RAD51 recruitment to ICL-stripes already 15 min after treatment (Figures 1B and 1C). At this time point, RAD51 recruitment is largely confined to replicating (EdU+) cells (Figure 1D). Overall, these data suggest that, using (DIG-)TMP/UVA, we can monitor induction and repair of ICLs and associated DSBs. Furthermore, they suggest that early recruitment of RAD51, preceding ICL-associated DSBs
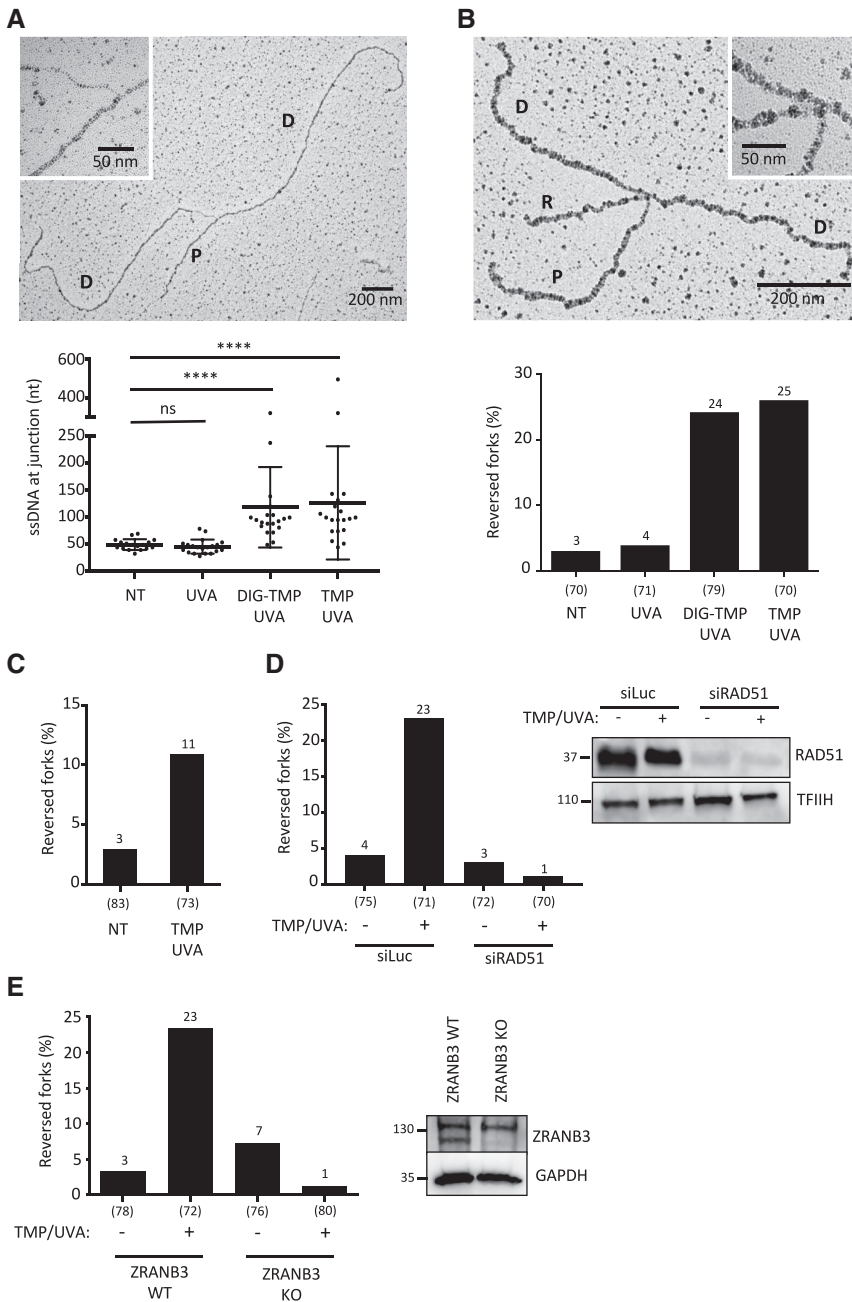
Figure 3. ICLs Rapidly Induce Frequent Fork Reversal, Mediated by RAD51 and ZRANB3

(A) Quantification of single-stranded DNA (ssDNA) at the replication junction by electron microscopy (EM). Representative image of a normal replication fork with magnification of the ssDNA region of interest (top). P, parental strand; D, daughter strand. Statistical analysis of ssDNA tract length in U2OS cells, optionally treated with either UVA alone (3 J/cm^2), or DIG-TMP (5 μM) and UVA (3 J/cm^2), or TMP (30 nM) and UVA (300 mJ/cm^2), and collected 1 hr post-treatment for analysis (bottom). Kruskal-Wallis test (****p < 0.0001; ns, not significant). Error bars indicate SD.

(B) Quantification of reversed replication forks by EM in U2OS cells treated as in (A). Representative image of a reversed fork (top) and statistical analysis (bottom). P, parental strand; D, daughter strand; R, regressed arm.

(C) Quantification of reversed forks in U2OS cells treated with TMP/UVA as in (A) but collected already 15 min post-irradiation.

(D) Percent reversed forks detected by EM in U2OS cells transfected with siLuc (control) or siRAD51 and treated optionally with TMP /UVA as in (A) (left). Western blot showing the downregulation of RAD51 protein levels (right). TFIIH, loading control.

(E) Percentage of reversed forks in ZRANB3-proficient (ZRANB3 wild-type [WT]) and ZRANB3-deficient (ZRANB3 KO) U2OS cells, which were optionally treated with TMP /UVA as in (A) (left). Western blot showing the absence of the ZRANB3 protein in ZRANB3-KO U2OS cells (right). GAPDH, loading control.

(A–E) A minimum of 70 forks were analyzed in two independent experiments. See also Table S1.

ture. This approach allows monitoring ssDNA accumulation and/or the conversion of replication forks into four-way junctions, known as reversed forks (Ray Chaudhuri et al., 2012; Zellweger et al., 2015). Both TMP and DIG-TMP treatments—coupled to UVA irradiation—lead to significant accumulation of ssDNA at replication forks (Figure 3A), which is a known marker of replication stress (Saldivar et al., 2017). Also, both treatments lead to the reversal of 20%–25% of the forks (Figure 3B; Table S1A). This cellular response is remarkably fast, as an increase in reversed fork frequency over background levels was observed as early as 15 min after treatment (Figure 3C; Table S1B). The central recombinase RAD51 and the DNA translocase ZRANB3 have been recently shown to mediate fork reversal using different genotoxic treatments and multiple genetic tools (Vujanovic et al., 2017; Zellweger et al., 2015). Using the same experimental setup, we confirmed that both factors are also strictly required for reversed fork formation upon treatment with ICL-inducing agents (Figures 3D and 3E; Tables S1C and

(Figure 2B). Remarkably, the population of *global* (undamaged) forks in treated cells also showed slower fork progression compared to forks from untreated cells. Along with the data in Figure 2A, these results suggest that a signaling mechanism induces global fork slowing throughout the nuclei of DIG-TMP/UVA-treated cells.

ICLs Rapidly Induce Frequent Fork Reversal, Dependent on RAD51 and ZRANB3

We next used psoralen cross-linking coupled to EM (Zellweger and Lopes, 2018) to investigate *in vivo* replication fork architec-
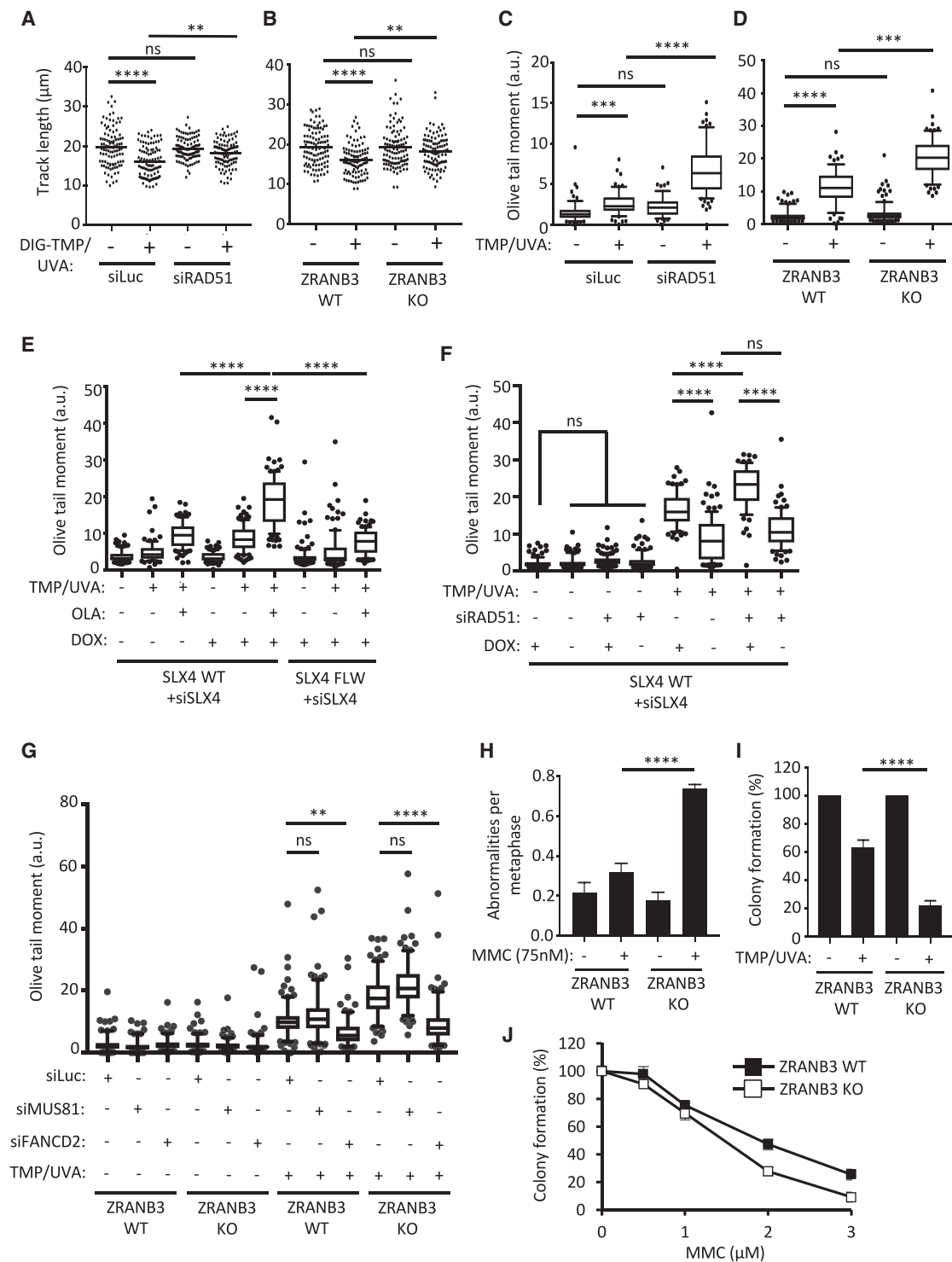
Figure 4. Impairing Fork Reversal Globally Affects Fork Slowing and Leads to ICL Incision-Dependent Breaks

(A and B) DNA fiber analysis (as in Figure 2B) in U2OS cells transfected with siLuc (control) or siRAD51 (A) or that were proficient (ZRANB3 WT) or deficient for ZRANB3 (ZRANB3 KO) (B). A minimum of 100 tracts was measured per sample. Kruskal-Wallis test (****p < 0.0001; **p < 0.01, 05; ns, not significant).

(C and D) Quantification of the olive tail moment by neutral comet assay in U2OS cells transfected with siLuc or siRAD51 (C) or in either ZRANB3 WT or ZRANB3 KO U2OS cells (D)—both optionally treated with TMP (30 nM) and UVA (300 mJ/cm^2).

(legend continued on next page)

S1D). These results also suggest that the fast recruitment of RAD51 to ICLs observed in replicating cells (Figures 1C and 1D) likely mediates prompt fork remodeling, as opposed to HR repair of ICL-associated DSBs.

Fork Reversal Mediates Global Fork Slowing and Limits ICL Incision-Dependent DSBs

Restraining replication fork progression was recently reported as a key function of FA factors in response to ICL (Lachaud et al., 2016). Active fork slowing upon genotoxic stress has been previously linked to replication fork reversal (Vujanovic et al., 2017; Zellweger et al., 2015). As we now report that fork slowing is not limited to damaged forks, but extends to undamaged forks throughout the nucleus (Figure 2), we assessed a potential role of fork reversal in ICL-induced global fork slowing. Using the experimental conditions described above, we performed DNA fiber assays in U2OS cells upon inactivation of RAD51 or ZRANB3, and found that both conditions impairing fork reversal also significantly affected global fork slowing upon DIG-TMP/UVA treatment (Figures 4A and 4B). Moreover, PARP inhibition—which was also reported to affect reversed fork accumulation (Berti et al., 2013; Ray Chaudhuri et al., 2012; Zellweger et al., 2015)—led to unrestrained fork progression upon ICL induction (Figure S4A). Neutral comet assays revealed that all of these genetic conditions of impaired fork slowing and reversal were consistently associated with a significant increase of chromosomal breakage early after TMP/UVA treatment (1 hr; Figures 4C–4E). Similar results were obtained when RAD51 inactivation was performed by a different small interfering RNA (siRNA) or in the untransformed RPE-1 cell line (Figures S4B and S4C).

We next used stable U2OS-derived cell lines to downregulate and conditionally re-express wild-type or mutant SLX4 (Guervilly et al., 2015)—a key nuclease scaffold regulating ICL incision activities (Klein Douwel et al., 2014)—and found that the increased chromosomal breakage observed upon impaired fork slowing and reversal depends on SLX4 and on its functional interaction with the XPF nuclease (Figures 4E, 4F, S4D, and S4E), both of which are strictly required for ICL unhooking (Klein Douwel et al., 2014). Accordingly, the accumulation of ICL-associated breaks in ZRANB3-defective cells depends on the ICL-processing factor FANCD2, but not on MUS81 (Figures 4G and S4F), which is dispensable for ICL unhooking (Klein Douwel et al., 2014). These results suggest that fork reversal mediates global fork slowing and prevents SLX4/XPF-dependent DSB formation at *local* forks by deregulated ICL unhooking. In keeping with these results, we found that ZRANB3 is required to limit chromo-

somal abnormalities upon ICL-inducing treatments (MMC; Figure 4H)—as previously shown for other DNA-damaging agents (Ciccia et al., 2012; Yuan et al., 2012)—and significantly contributes to cell survival upon MMC or TMP/UVA treatments (Figures 4I and 4J). Overall, these data support the relevance of replication fork remodeling for genome integrity and cell survival upon ICL induction.

Fork Reversal Promotes ICL Traverse, Independently of FANCM

We further assessed how replication fork remodeling contributes to ICL replication, focusing on the forks directly challenged by the lesions. We used the DNA fiber assays coupled to DIG-TMP treatment and detection (Huang et al., 2013), and confirmed in U2OS cells that around 60% of the forks are able to traverse through ICLs as single forks, while a minority of forks is either transiently stalled at the lesion ($\approx$25%) or converging at the lesion with a second fork ($\approx$15%) (Figure 5A) (Huang et al., 2013). ICL traverse is also very efficient in mouse embryonic fibroblasts and does not require a specific glycosylase (i.e., Neil3; Figure S4G), which was recently shown to provide an alternative ICL-unhooking mechanism in *Xenopus* egg extracts (Semlow et al., 2016). Inactivation of either RAD51 or ZRANB3 led to a significant increase in replication fork stalling and a parallel decrease in ICL traverse, while the frequency of converging forks was unchanged (Figures 5B and 5C). Thus, global fork slowing and reversal is required for efficient ICL traverse.

As ICL traverse was shown to depend on the DNA translocase FANCM (Huang et al., 2013)—which is capable of reversing synthetic forks in biochemical experiments (Gari et al., 2008)—we directly assessed its contribution by effective siRNA-mediated downregulation. As reported (Huang et al., 2013), FANCM depletion affected ICL traverse, to a similar extent as RAD51 or ZRANB3 inactivation (Figures 5B–5D). However, neither ICL-induced fork reversal nor global fork slowing were affected by FANCM depletion (Figures 5E, S4H, and S4I; Table S2). These data suggest that global fork slowing and reversal occur upstream of ICL traverse and that FANCM promotes ICL traverse via alternative transactions occurring locally at ICL-damaged forks.

ICL Traverse Can Be Visualized as Postreplicative Sister Chromatid Junctions, Resolved by ICL Incision

An important implication of ICL traverse by single forks is that ICL unhooking should frequently occur post-replicatively—i.e., after ICL traverse—allowing to physically separate replicated

---

(E) FIT-inducible SLX4 WT and SLX4 FLW cells, transfected with siRNA against 3′ UTR of endogenous SLX4, and, where indicated, treated with Dox (1 ng/mL) in order to express exogenous SLX4 wild-type (SLX4 WT) or mutant (SLX4 FLW) protein. All cells were optionally treated with TMP/UVA (as in C), PARP inhibitor (Olaparib [OLA]; 10 μM), and processed for neutral comet assays.

(F) FIT-inducible SLX4 wild-type cells were transfected with siRNA against 3′ UTR of SLX4 and siLuc or siRAD51 and, 20 hr later, incubated with Dox for 16 hr. Cells were optionally treated as in (C) and processed for neutral comet assays.

(G) ZRANB3 WT or ZRANB3 KO U2OS cells were transfected with siLuc, siMUS81, or siFANCD2. 48 hr later, the cells were optionally treated as in (C) and processed for neutral comet assay. In (C)–(G), at least 50 comets were scored per sample. Kruskal-Wallis test (****p < 0.0001; ***p < 0.001; ns, not significant).

(H) Number of chromosomal abnormalities per indicated cell line, as determined by metaphase spreading upon optional 20-hr MMC treatment (75 nM), followed by 16-hr nocodazole treatment (200 ng/mL).

(I and J) ZRANB3 WT or ZRANB3 KO U2OS cells were left untreated or treated with TMP (30 nM) plus UVA (300 mJ/cm^2) (I) or treated for 8 hr with the indicated doses of MMC (J) to assess colony formation.

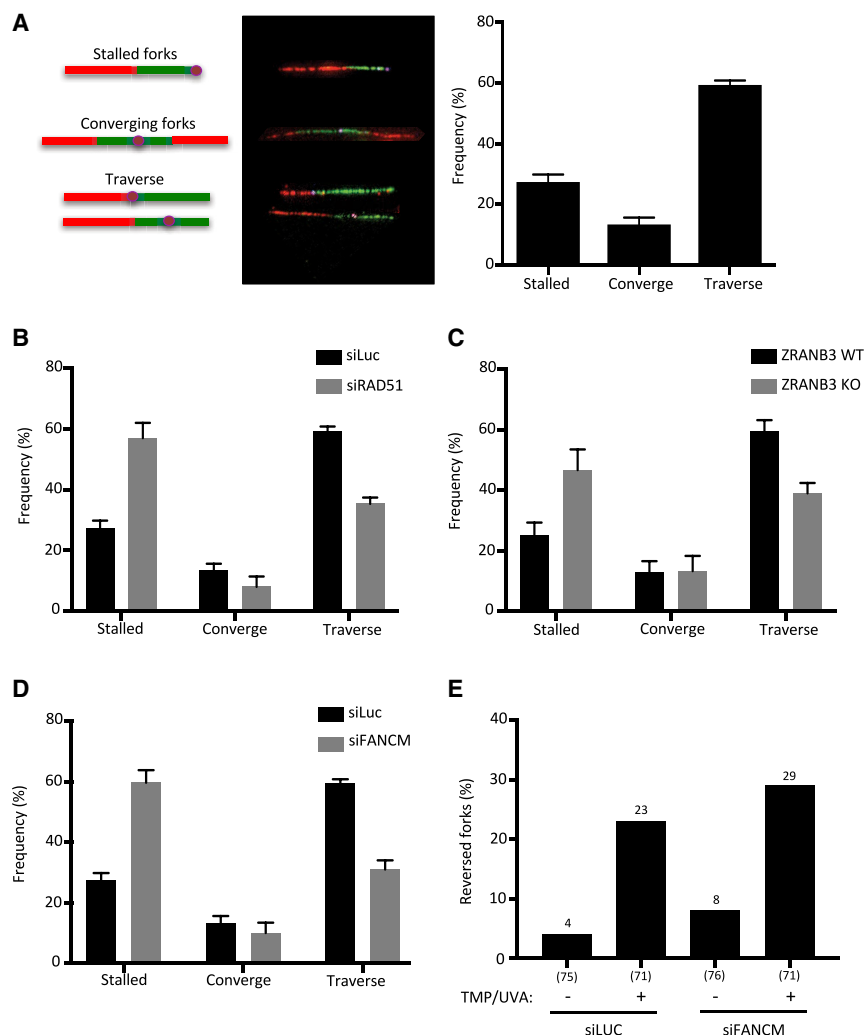(H–J) Error bars indicate SD. See also Figure S4.

Figure 5. Fork Reversal Promotes ICL Traverse in a FANCM-Independent Manner

(A) DNA fiber tracks were generated as in Figure 2B. Schematic display of local replication patterns containing an ICL (DIG-label, pink)—such as stalled forks, converging forks, and fork traverse (left). Representative images of local replication patterns (middle). Frequency of the replication patterns observed in local forks (right). A minimum of 100 tracts was analyzed per experiment.

(B) Frequency of local replication patterns (as in A) in U2OS cells transfected with siLuc or si RAD51.

(C) Frequency of local replication patterns (as in A) in ZRANB3 WT or ZRANB3 KO cells.

(D) Frequency of local replication patterns (as in A) in U2OS cells transfected with siLuc (control) or with an siFANCM. In (B)–(D), a minimum of 100 forks was analyzed.

(E) Percentage of reversed forks detected by EM in U2OS cells transfected with siLuc (control) or si-FANCM—treated 48-hr post transfection with TMP (30 nM) and UVA (300 mJ/cm^2). Cells were collected 1 hr after irradiation. A minimum of 70 forks were analyzed in two independent experiments.

(A–D) Error bars indicate SD. See also Figure S4 and Table S2.

duplexes behind the forks. Evidence for this has been so far limited to multicolor DNA fiber experiments performed in Chinese hamster cells (Huang et al., 2013). We thus set out to provide direct visualization of ICL traverse in human cells and to study the role of ICL unhooking in fork transactions at ICLs. Using DNA fiber and EM analysis, we found that abolishing ICL unhooking by SLX4 downregulation had no visible effect on the efficiency of ICL traverse or on the frequency of TMP/UVA-induced reversed forks, suggesting that ICL unhooking does not contribute to global fork remodeling or ICL replication bypass (Figures 6A and 6B; Table S3). We then carefully inspected the architecture of replication forks upon TMP/UVA treatment, performing our EM analysis with low DNA concentration, to minimize accidental inter- or intra-molecular crossings of DNA strands. ICL traverse events are expected to move ICLs behind replication forks, resulting in detectable sister chromatid junctions at symmetric distance from the fork (postreplicative junctions [PRJs]; Figure 6C) or in symmetric X-shaped molecules (Figure 6D), when fork and junction are separated by restriction digestion. In these experimental conditions, crossings of repli-

cated duplexes behind forks (postreplicative junctions) or X-shaped molecules were extremely rare in untreated cells (<1%; Figure 6E; Table S4). Furthermore, the rare four-way junctions identified in untreated cells displayed contour-length measurements expected for reversed forks (Figures 6B)—i.e., only two of the four arms equal in length, as typically observed in 3%–5% of the forks in untreated U2OS cells (Zellweger and Lopes, 2018; Zellweger et al., 2015). Although reversed forks expectedly increased upon TMP/UVA treatment, both postreplicative junction and symmetric X-molecules were only rarely observed in control U2OS cells (2%–3%; Figures 6B and 6E; Tables S3 and S4). However, when ICL unhooking was prevented by SLX4 depletion, ≈7% of replication forks (20 out of 295 intermediates) in TMP/UVA-treated cells displayed a junction between replicated duplexes, positioned at symmetric distance from the fork (postreplicative junctions; Figures 6C, 6E, and S5A–S5D; Table S4). Analogously, besides ICL-induced reversed forks (Figure 6B), several additional four-way junctions (≈3%, 9 out of 295 intermediates) were observed in TMP/UVA-treated SLX4-depleted cells and displayed symmetric length of the four arms (Xs; Figures 6D, 6E, and S5E–S5H; Table S4). These observations strongly suggest that forks efficiently traverse ICLs in human cells, generating sister chromatid junctions (postreplicative junctions + Xs) that are rapidly resolved by SLX4-dependent ICL unhooking. Accordingly, these molecules accumulated in TMP/UVA-treated cells also upon XPF inactivation, but not upon MUS81 defects (Figures 6F and S6A; Table S5), reflecting the different contribution of these nucleases to ICL
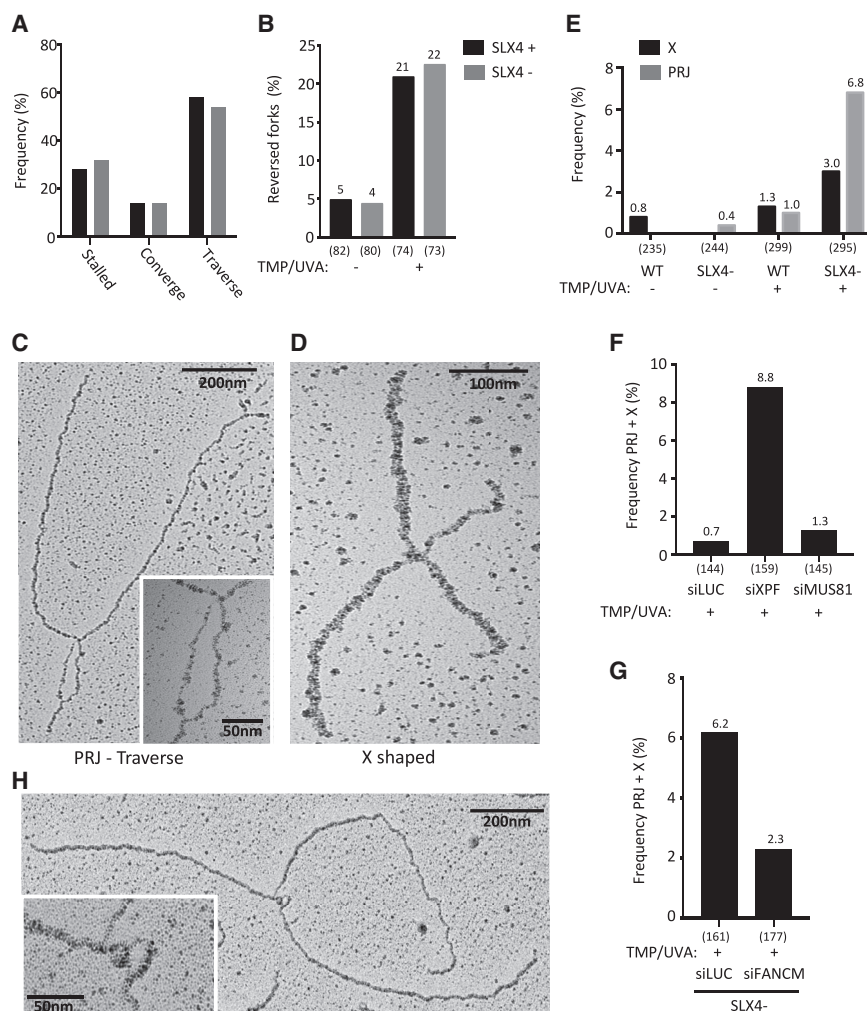
Figure 6. Visualization of ICL Traverse as Postreplicative Sister Chromatid Junctions, Resolved by ICL Incision

(A) Frequency of local replication patterns (as in Figure 5A) in FIT-inducible SLX4 proficient (SLX4+) or deficient (SLX4−) cells (as in Figure 4E). A minimum of 100 forks was analyzed per experiment.

(B and E) Frequency of local replication patterns determined by EM, such as reversed forks (B), postreplicative junctions (PRJs) and X-shaped molecules (E) in SLX4+ and SLX4− cells that were either left untreated or treated with TMP/UVA (30 nM/300 mJ/cm^2). A minimum of 70 forks was analyzed per sample in two independent experiments.

(C and D) Representative electron micrograph showing a postreplicative junction behind a replication fork, indicative of ICL traverse (C) or an X-shaped molecule (D).

(F) Total frequency of postreplicative junction + X-shaped molecules from U2OS cells, transfected with siLuc, siXPF, or siMUS81 and treated with TMP/UVA (30 nM/300 mJ/cm^2). A minimum of 70 forks was analyzed per sample in two independent experiments.

(G) Total frequency of postreplicative junction + X-shaped molecules in SLX4− cells (as in Figure 4E) transfected with siLuc or siFANCM and treated with TMP (30 nM) and UVA irradiated (300 mJ/cm^2). A minimum of 70 forks was analyzed per sample.

(H) Representative image showing a postreplicative junction behind a replication fork, indicative of ICL traverse. ICL labeled with an antibody against DIG. See also Figures S5 and S6 and Tables S3–S6.

unhooking (Klein Douwel et al., 2014). Furthermore, postreplicative junction+X accumulation in TMP/UVA-treated SLX4-defective cells was largely dependent on FANCM (Figure 6G; Table S6), which was previously shown to mediate efficient ICL traverse (Huang et al., 2013). Finally, we optimized experimental conditions for the specific binding of a gold-conjugated anti-DIG antibody to genomic DNA extracted from DIG-TMP/UVA-treated cells, in order to directly reveal ICLs at individual intermediates (Figures S6B–S6D). Only a fraction of ICL-containing molecules is efficiently bound by the antibody, and we cannot exclude a bias toward/against binding of specific intermediates, which prevents using this method for quantitative analyses. However, we did observe antibody binding at a subset of replication intermediates consistent with fork stalling/convergence at ICLs (Figures S6E and S6F). Importantly—although the complex architecture of ICL traverse intermediates favored in vitro intramolecular interactions and antibody clumping (Figure S6G), preventing reliable identification of several traverse intermediate candidates—it was occasionally possible to observe antibody binding also at postreplicative junctions behind a replication fork (Figure 6H). Altogether, the available set of EM data suggests that ICL traverse is frequent and can be directly visualized in human cells.

ATR Modulates Global Fork Slowing and Reversal upon ICL Induction and Other Genotoxic Treatments

The reduction in DNA synthesis reported above upon ICL induction is accompanied by replication fork slowing and reversal, and by a parallel increase in γH2AX in replicating cells, suggesting a role for ATR-dependent signaling in these mechanisms. ATR inhibition by AZ20 (Foote et al., 2013) expectedly increased EdU incorporation, likely reflecting unleashed origin firing (Karnani and Dutta, 2011). Indeed, by preventing de novo origin firing, CDC7 inhibition by XL413 suppresses this effect and allows focusing on the effects of ATR inhibition on ongoing forks (Figures 7A, S7A, and S7B). In these experimental conditions, TMP/UVA treatment reduced DNA synthesis by limiting the progression of active forks. Remarkably, this effect was completely abolished by ATR inhibition (Figure 7B), which also suppressed TMP/UVA-induced γH2AX, despite comparable levels of induced ICLs (Figures 7C and S7C–S7E). Very similar observations were made measuring EdU incorporation at a distance
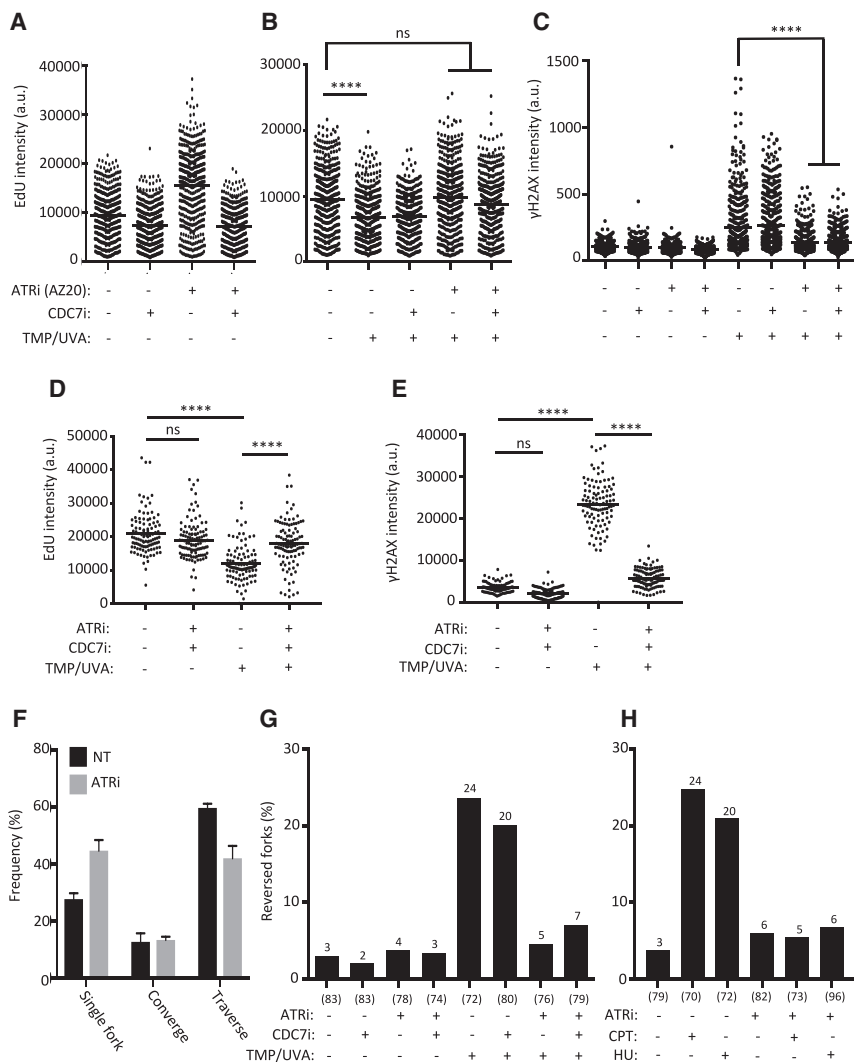
Figure 7. ATR Modulates Global Fork Slowing and Reversal upon ICL Induction and Other Genotoxic Treatments

(A and B) EdU incorporation by FACS analysis: U2OS cells were incubated for 30 min without (A) or with (B) TMP (30 nM), AZ20 (ATR inhibitor, 1 μM), CDC7i (XL413, 10 μM), or in all possible combinations of the three, followed by irradiation with UVA (300 mJ/cm²). EdU (10 μM) incorporation was allowed for 30 min in the presence or absence of AZ20 (ATR inhibitor, 1 μM), CDC7i (XL413, 10 μM), or both. EdU intensity values in S-phase cells were extracted for a minimum of 400 random cells per sample. Kruskal-Wallis test (****p < 0.0001; ns, not significant).

(C) Cells were treated as in (A) and (B) and stained with an antibody against γH2AX. γH2AX intensity values from 400 random S-phase cells were extracted. Kruskal-Wallis test (****p < 0.0001).

(D and E) U2OS cells were incubated with or without DIG-TMP (5 μM), AZ20 (ATR inhibitor, 1 μM), and CDC7i (XL413, 10 μM) for 30 min in the indicated combinations. Cells were irradiated using a UVA laser. EdU Click-iT and IF was performed for EdU and γH2AX, respectively. EdU (D) and γH2AX (E) intensities in ROIs (as described in Figure 2A) were determined using ImageJ.

(F) DNA fiber analysis of local replication patterns (displayed in Figure 5A) was combined with the presence or absence of ATR inhibitor (AZ20, 1 μM). Error bars indicate SD.

(G) Percentage of reversed forks assessed by EM in untreated U2OS cells or cells treated with TMP (30 nM), AZ20 (ATR inhibitor, 1 μM), CDC7i (XL413, 10 μM), or in all possible combination of the three. A minimum of 70 forks was analyzed in two independent experiments.

(H) Percentage of reversed forks assessed by EM in U2OS cells left untreated or pre-incubated for 30 min with ATR inhibitor (AZ20, 1 μM). Following pre-incubation, cells were treated, where indicated, with camptothecin (CPT) (25 nM) or hydroxyurea (HU) (500 μM) for 1 hr. A minimum of 70 forks was analyzed in two independent experiments. See also Figure S7 and Table S7.

from laser-induced ICL stripes, using the approach described in Figure 2A. Also, in this case, ATR inhibition impaired H2AX phosphorylation and triggered unrestrained DNA synthesis in laser-irradiated nuclei, despite simultaneous inhibition of CDC7, and thus independently of *de novo* origin firing (Figures 7D and 7E). Analogous results on DNA synthesis and γH2AX were obtained combining CDC7 inhibition with a second ATR inhibitor (VE821; Figures S7F and S7G). As for all other conditions impairing global fork slowing (Figures 4 and 5), ATR inhibition also impaired efficient ICL traverse at local forks (Figure 7F).

As we observed a tight association between global fork slowing, ICL traverse, and fork reversal (Figure 4), we directly assessed by EM the effect of ATR inhibition on fork reversal upon ICL induction. ATR inhibition completely suppressed TMP/UVA-induced fork reversal, even when unscheduled origin firing was prevented by CDC7 inhibition (Figure 7G; Table S7A). We next tested whether ATR role in fork reversal extended to other conditions of replication interference, previously reported to

induce frequent fork remodeling (i.e., topoisomerase I inhibition by camptothecin [CPT]; nucleotide depletion by hydroxyurea [HU]) (Zellweger et al., 2015). Upon all tested treatments, ATR inhibition completely abolished drug-induced fork reversal (Figure 7H; Table S7B). Collectively, these results suggest that ATR activation upon various types of replication stress generates an active signal to promote global fork slowing and reversal, which extends to forks that are not directly challenged by DNA lesions.

DISCUSSION

Replication fork reversal was previously reported as a general response to multiple genotoxic treatments, including ICL-inducing agents like cisplatin and MMC (Zellweger et al., 2015). Albeit not surprising, the observation that fork reversal occurs frequently upon (DIG-)TMP/UVA treatments is important to understand ICL replication and processing in human cells, as these

compounds induce a much higher ICL/monoadduct (MA) ratio than cisplatin or MMC (Huang et al., 2013; Lai et al., 2008). Furthermore, DIG-TMP treatment provides a unique opportunity to distinguish forks directly challenged by ICLs (*local* forks) from those that do not encounter ICLs (*global* forks), enabling assessment of the relevance of fork slowing and reversal in both contexts. In our experimental conditions, only ≈10% of the forks replicate across an ICL within 1 hr after treatment (Figures S3C and S3D). Of these, only ≈25% (i.e., 2.5% of total forks) are stalled at ICLs at any given time (Figure 5A). Based on the frequency of reversed forks observed in the same experimental conditions (20%–25% of total forks), we conclude that the vast majority of reversal events occur at a distance from ICL. We propose that fork reversal mostly occurs as a result of a signaling mechanism—emanating from the damage itself, its processing, and/or the first few forks dealing with it—ultimately involving a high fraction of the forks. In light of the tight association between fork reversal and fork slowing observed here and in previous studies (Kile et al., 2015; Ray Chaudhuri et al., 2012; Vujanovic et al., 2017; Zellweger et al., 2015), we envision global fork reversal as a molecular switch to provide more time for the template to be repaired before duplication by ongoing forks. This cellular response may be particularly relevant in face of ICLs, as their removal requires DNA incision events that are potentially risky in close vicinity to replication forks. ICL recognition and repair were previously shown to occur on non-replicating dsDNA (Williams et al., 2013). In fact, biochemical evidence suggests that ICL unhooking by SLX4/XPF may be inhibited next to stalled forks and require RPA recruitment to exposed ssDNA (Abdullah et al., 2017). We thus propose that global fork reversal promotes ICL repair on the double-stranded template by transiently delaying global fork progression, thereby avoiding untimely and excessive ICL encounters by forks and limiting SLX4-dependent fork breakage (Figure S7H, I–III). As replication-independent ICL repair was shown to activate ATR in *Xenopus* egg extracts (Williams et al., 2013), it will be important to assess whether in human cells this pathway is also active in S phase and liaises with ATR-mediated control of fork progression.

While assisting template repair and limiting dangerous fork processing events, active slowing and reversal appears to mediate also efficient ICL traverse by those forks that meet unrepaired ICLs (Figure S7H, IV). By EM analysis in SLX4-defective cells, we provide here direct visualization of these ICL traverse intermediates as postreplicative junctions of daughter duplexes behind moving forks (postreplicative junction+Xs; Figure 6). The low number of these junctions observed in SLX4-proficient cells—and their preferential visualization in close proximity to forks (i.e., postreplicative junction > Xs)—suggest that the kinetics of postreplicative ICL unhooking is very fast and mechanistically coupled with ICL traverse. We propose that efficient ICL traverse promotes ICL unhooking on postreplicative dsDNA and helps uncoupling ICL processing from the forks, thereby limiting potentially cytotoxic fork breakage (Figure S7H, V and VI). Furthermore, performing ICL repair at postreplicative junctions may be coupled to strand annealing events, in order to limit DSB formation upon ICL incision (Figure S7H, VII and VIII), as already proposed at

converging forks (Zhang and Walter, 2014). While these fork remodeling-associated ICL tolerance mechanisms provide only a limited contribution to the resistance of wild-type cells to ICL-inducing treatments (Figure 4J), they may represent crucial modulators of chemosensitivity upon hypomorphic DSB repair defects, which are frequently found in tumors and limit ICL repair capacity.

It is currently unclear whether, besides global regulation of fork progression, fork remodeling in proximity to the lesions may also participate directly in the mechanism of ICL traverse or in promoting fork fusion at ICLs. In the context of fork fusion—which is rapidly observed at all ICL-containing plasmids replicating in *Xenopus* egg extracts (Räschle et al., 2008)—fork reversal was recently shown to follow replisome disassembly and, similarly to what proposed above for single ongoing forks, may promote ICL processing on the reannealed parental duplex (Amunugama et al., 2018). On human chromosomes, where most ICLs are bypassed by single forks (Figure 5) (Huang et al., 2013), fork reversal may in principle promote the required reorganization and/or translocation of replisome components across the ICL to assist fork restart beyond the ICL. By extending the linear DNA duplex between the fork junction and the ICL, fork reversal might prime replicative helicase remodeling from an ssDNA to a dsDNA configuration, thus allowing its sliding past the lesion, as previously suggested (Huang et al., 2013). Similarly, although we propose that ATR assists ICL traverse by promoting fork reversal, our data do not exclude direct ATR-dependent modifications of the replisome and accessory proteins, to mediate template unwinding and fork restart beyond ICLs. Assessing directly the role of ATR and the relevance of fork reversal in ICL traverse will require careful biochemical reconstitution of the traverse reaction.

FANCM was previously shown to remodel forks in biochemical assays (Gari et al., 2008) and was reported to promote efficient ICL traverse (Huang et al., 2013). While our data confirm the role of FANCM in ICL traverse, it also excludes a detectable contribution to global fork slowing and reversal in human cells. These data further suggest that replication fork reversal occurs upstream of ICL traverse and that FANCM may be involved in a specialized fork restart pathway enabling ICL traverse from previously reversed forks. This hypothesis is consistent with the reported defect of FANCM-defective cells in restarting stalled forks (Schwab et al., 2010) and will require further investigation.

Previous parallel analyses of fork architecture and checkpoint activation in response to several genotoxic treatments had failed to find linear correlations between replication fork reversal and detectable activation of the ATR or ATM pathways (Zellweger et al., 2015). It should be noted, however, that activation of ATR/ATM was assessed monitoring phosphorylation events on specific targets (CHK1 and KAP1, respectively), which may not be necessarily relevant for ATR-mediated regulation of fork progression. In keeping with this, FANCM-defective cells are reportedly inefficient in global ATR signaling—e.g., CHK1-, p53-, or SMC1 phosphorylation (Collis et al., 2008; Huang et al., 2010; Schwab et al., 2010)—but displayed no defect in global fork slowing and reversal in our study. A direct link between ATR activation and slower progression of ongoing forks has been difficult

to assess, mainly because of the reported effects on origin firing and its indirect impact on fork progression (Petermann et al., 2006, 2010). Uncoupling the two effects by simultaneous CDC7 inhibition, and monitoring directly damaged and undamaged forks by DIG-TMP detection, we now report that ATR activity promotes fork slowing and reversal of a large fraction of replication forks, including those that are not directly challenged by ICLs. As we observed similar effects on fork reversal upon different types of replication stress, it is most likely that this ATR-mediated cross talk between damaged and undamaged forks is part of a general response to genotoxic stress, possibly related to the recently reported metabolic control of fork progression rates (Somyajit et al., 2017). Our observations open the exciting perspective of exploring alternative ATR targets regulating progression and stability of ongoing forks. In light of the high number of reported ATR targets among replisome components, accessory factors, and HR proteins (Ahlskog et al., 2016; Errico and Costanzo, 2012; Lossaint et al., 2013; Murphy et al., 2014; Somyajit et al., 2013; Vassin et al., 2009), this open question should be tackled thoroughly in a new exciting avenue of research.

Intriguingly, fork reversal was reported to be increased at stalled forks upon inactivation of the yeast replication checkpoint kinase Rad53 (Sogo et al., 2002). It should be noted, however, that fork reversal in yeast is abundant only upon topoisomerase I inhibition (Ray Chaudhuri et al., 2012), and that an increase in checkpoint-defective cells is only clearly detected upon nucleotide depletion (Lopes et al., 2006; Sogo et al., 2002). Similarly, ATR inhibition in human cells was shown to induce SMARCAL1-dependent exposure of native ssDNA, which was interpreted as accumulation of reversed forks with paired nascent strands of unequal length (Couch et al., 2013). However, this was observed only upon prolonged nucleotide depletion and simultaneous deregulation of origin firing by ATR inhibition. In both contexts, reversed forks and/or other intermediates exposing nascent ssDNA may accumulate as a pathological consequence of massive ssDNA accumulation—which was found to directly correlate with reversed fork frequency (Zellweger et al., 2015)—rather than reflecting an active role of the replication checkpoint in preventing fork remodeling upon genotoxic stress.

How is ATR initially activated, to spread a signal for global fork reversal? An accumulation of ssDNA at replication forks is detectable upon all tested genotoxic treatments (Figure 3) (Zellweger et al., 2015). This may reflect uncoupled DNA synthesis and/or regulated fork resection in proximity to DNA lesion, and may well account for initial ATR activation. However, it is also possible that intermediates of ICL processing ahead or behind replication forks contribute to boost ATR activation and phosphorylation of the relevant targets. Interestingly, fork reversal observed in unperturbed cells—likely occurring at endogenous difficult-to-replicate regions—is uncoupled from globally detectable ATR signaling and H2AX phosphorylation (Figure 7H) (Schmid et al., 2018).

Our data may be relevant in light of the promise of ATR inhibitors in cancer chemotherapy. We note that unrestrained fork progression and defective fork reversal upon replication stress are induced by both PARP (Ray Chaudhuri et al., 2012) and ATR inhibitors (this study), both of which hold great promise as therapeutic agents, particularly in combination with other genotoxic treatments. It is thus tempting to speculate that both treatments affect crucial fork protection mechanisms, thereby promoting DSB accumulation upon endogenous or exogenous replication stress. The identification of key ATR targets or separation-of-function mutations will allow testing the specific contribution of this function of the ATR checkpoint in the promising cytotoxicity observed in cancer cells upon ATR inhibition.

Finally, our data suggest that combining DIG-TMP/UVA-based DNA fiber-spreading and comet assays may be highly predictive of cancer-specific responses to chemotherapeutic regimens with ICL-inducing agents. Testing this possibility in relevant patient-derived samples may pave the way to use functional replication tests as standard predictive assays for personalized medicine in clinical oncology.

STAR★METHODS

Detailed methods are provided in the online version of this paper and include the following:

- KEY RESOURCES TABLE
- CONTACT FOR REAGENT AND RESOURCE SHARING
- EXPERIMENTAL MODEL AND SUBJECT DETAILS
- METHOD DETAILS
  - Cell Culture and Cell Lines
  - Transfections of siRNA Oligos
  - Drug Treatments
  - DNA Fiber Analysis
  - Immunofluorescence
  - FACS Analysis
  - Neutral Comet Assay
  - Western Blotting
  - Electron Microscopy
  - Chromosomal Breakage and Abnormalities by Metaphase Spreading
  - Cell Survival by Colony Formation
  - Quantification and Statistical Analysis
  - Chemical Synthesis of DIG-TMP

AUTHOR CONTRIBUTIONS

DECLARATION OF INTERESTS

SUPPORTING CITATIONS

The following references appear in the Supplemental Information: Braun et al. (2004); Isaacs et al. (1977); Thazhathveetil et al. (2007).

REFERENCES

Abdullah, U.B., McGouran, J.F., Brolih, S., Ptchelkine, D., El-Sagheer, A.H., Brown, T., and McHugh, P.J. (2017). RPA activates the XPF-ERCC1 endonuclease to initiate processing of DNA interstrand crosslinks. EMBO J. 36, 2047–2060.

Ahlskog, J.K., Larsen, B.D., Achanta, K., and Sørensen, C.S. (2016). ATM/ATR-mediated phosphorylation of PALB2 promotes RAD51 function. EMBO Rep. 17, 671–681.

Amunugama, R., Willcox, S., Wu, R.A., Abdullah, U.B., El-Sagheer, A.H., Brown, T., McHugh, P.J., Griffith, J.D., and Walter, J.C. (2018). Replication fork reversal during DNA interstrand crosslink repair requires CMG unloading. Cell Rep. 23, 3419–3428.

Berti, M., and Vindigni, A. (2016). Replication stress: getting back on track. Nat. Struct. Mol. Biol. 23, 103–109.

Berti, M., Ray Chaudhuri, A., Thangavel, S., Gomathinayagam, S., Kenig, S., Vujanovic, M., Odreman, F., Glatter, T., Graziano, S., Mendoza-Maldonado, R., et al. (2013). Human RECQ1 promotes restart of replication forks reversed by DNA topoisomerase I inhibition. Nat. Struct. Mol. Biol. 20, 347–354.

Braun, M., Hartnagel, U., Ravanelli, E., Schade, B., Böttcher, C., Vostrowsky, O., and Hirsch, A. (2004). Amphiphilic [5:1]- and [3:3]-hexakisadducts of C60. Eur. J. Org. Chem. 2004, 1983–2001.

Ceccaldi, R., Sarangi, P., and D'Andrea, A.D. (2016). The Fanconi anaemia pathway: new players and new functions. Nat. Rev. Mol. Cell Biol. 17, 337–349.

Ciccia, A., Nimonkar, A.V., Hu, Y., Hajdu, I., Achar, Y.J., Izhar, L., Petit, S.A., Adamson, B., Yoon, J.C., Kowalczykowski, S.C., et al. (2012). Polyubiquitinated PCNA recruits the ZRANB3 translocase to maintain genomic integrity after replication stress. Mol. Cell 47, 396–409.

Collis, S.J., Ciccia, A., Deans, A.J., Horejsí, Z., Martin, J.S., Maslen, S.L., Skehel, J.M., Elledge, S.J., West, S.C., and Boulton, S.J. (2008). FANCM and FAAP24 function in ATR-mediated checkpoint signaling independently of the Fanconi anemia core complex. Mol. Cell 32, 313–324.

Costanzo, V., Shechter, D., Lupardus, P.J., Cimprich, K.A., Gottesman, M., and Gautier, J. (2003). An ATR- and Cdc7-dependent DNA damage checkpoint that inhibits initiation of DNA replication. Mol. Cell 11, 203–213.

Couch, F.B., Bansbach, C.E., Driscoll, R., Luzwick, J.W., Glick, G.G., Bétous, R., Carroll, C.M., Jung, S.Y., Qin, J., Cimprich, K.A., and Cortez, D. (2013). ATR phosphorylates SMARCAL1 to prevent replication fork collapse. Genes Dev. 27, 1610–1623.

Deans, A.J., and West, S.C. (2011). DNA interstrand crosslink repair and cancer. Nat. Rev. Cancer 11, 467–480.

Errico, A., and Costanzo, V. (2012). Mechanisms of replication fork protection: a safeguard for genome stability. Crit. Rev. Biochem. Mol. Biol. 47, 222–235.

Foote, K.M., Blades, K., Cronin, A., Fillery, S., Guichard, S.S., Hassall, L., Hickson, I., Jacq, X., Jewsbury, P.J., McGuire, T.M., et al. (2013). Discovery of 4-4-[(3R)-3-methylmorpholin-4-yl]-6-[1-(methylsulfonyl)cyclopropyl]pyrimidin-2-yl-1H-indole (AZ20): a potent and selective inhibitor of ATR protein kinase with monotherapy in vivo antitumor activity. J. Med. Chem. 56, 2125–2138.

Gari, K., Décaillet, C., Stasiak, A.Z., Stasiak, A., and Constantinou, A. (2008). The Fanconi anemia protein FANCM can promote branch migration of Holliday junctions and replication forks. Mol. Cell 29, 141–148.

Guervilly, J.-H., Takedachi, A., Naim, V., Scaglione, S., Chawhan, C., Lovera, Y., Despras, E., Kuraoka, I., Kannouche, P., Rosselli, F., and Gaillard, P.H. (2015). The SLX4 complex is a SUMO E3 ligase that impacts on replication stress outcome and genome stability. Mol. Cell 57, 123–137.

Guo, C., Kumagai, A., Schlacher, K., Shevchenko, A., Shevchenko, A., and Dunphy, W.G. (2015). Interaction of Chk1 with Treslin negatively regulates the initiation of chromosomal DNA replication. Mol. Cell 57, 492–505.

Huang, M., Kim, J.M., Shiotani, B., Yang, K., Zou, L., and D'Andrea, A.D. (2010). The FANCM/FAAP24 complex is required for the DNA interstrand crosslink-induced checkpoint response. Mol. Cell 39, 259–268.

Huang, J., Liu, S., Bellani, M.A., Thazhathveetil, A.K., Ling, C., de Winter, J.P., Wang, Y., Wang, W., and Seidman, M.M. (2013). The DNA translocase FANCM/MHF promotes replication traverse of DNA interstrand crosslinks. Mol. Cell 52, 434–446.

Isaacs, S.T., Shen, C.K., Hearst, J.E., and Rapoport, H. (1977). Synthesis and characterization of new psoralen derivatives with superior photoreactivity with DNA and RNA. Biochemistry 16, 1058–1064.

Karnani, N., and Dutta, A. (2011). The effect of the intra-S-phase checkpoint on origins of replication in human cells. Genes Dev. 25, 621–633.

Katsuno, Y., Suzuki, A., Sugimura, K., Okumura, K., Zineldeen, D.H., Shimada, M., Niida, H., Mizuno, T., Hanaoka, F., and Nakanishi, M. (2009). Cyclin A-Cdk1 regulates the origin firing program in mammalian cells. Proc. Natl. Acad. Sci. USA 106, 3184–3189.

Kile, A.C., Chavez, D.A., Bacal, J., Eldirany, S., Korzhnev, D.M., Bezsonova, I., Eichman, B.F., and Cimprich, K.A. (2015). HLTF's ancient HIRAN domain binds 3' DNA ends to drive replication fork reversal. Mol. Cell 58, 1090–1100.

Klein Douwel, D., Boonen, R.A.C.M., Long, D.T., Szypowska, A.A., Räschle, M., Walter, J.C., and Knipscheer, P. (2014). XPF-ERCC1 acts in unhooking DNA interstrand crosslinks in cooperation with FANCD2 and FANCP/SLX4. Mol. Cell 54, 460–471.

Kottemann, M.C., and Smogorzewska, A. (2013). Fanconi anaemia and the repair of Watson and Crick DNA crosslinks. Nature 493, 356–363.

Lachaud, C., Moreno, A., Marchesi, F., Toth, R., Blow, J.J., and Rouse, J. (2016). Ubiquitinated Fancd2 recruits Fan1 to stalled replication forks to prevent genome instability. Science 351, 846–849.

Lai, C., Cao, H., Hearst, J.E., Corash, L., Luo, H., and Wang, Y. (2008). Quantitative analysis of DNA interstrand cross-links and monoadducts formed in human cells induced by psoralens and UVA irradiation. Anal. Chem. 80, 8790–8798.

Langevin, F., Crossan, G.P., Rosado, I.V., Arends, M.J., and Patel, K.J. (2011). Fancd2 counteracts the toxic effects of naturally produced aldehydes in mice. Nature 475, 53–58.

Liu, H., Takeda, S., Kumar, R., Westergard, T.D., Brown, E.J., Pandita, T.K., Cheng, E.H.-Y., and Hsieh, J.J.-D. (2010). Phosphorylation of MLL by ATR is required for execution of mammalian S-phase checkpoint. Nature 467, 343–346.

Long, D.T., Räschle, M., Joukov, V., and Walter, J.C. (2011). Mechanism of RAD51-dependent DNA interstrand cross-link repair. Science 333, 84–87.

Long, D.T., Joukov, V., Budzowska, M., and Walter, J.C. (2014). BRCA1 promotes unloading of the CMG helicase from a stalled DNA replication fork. Mol. Cell 56, 174–185.

Lopes, M., Foiani, M., and Sogo, J.M. (2006). Multiple mechanisms control chromosome integrity after replication fork uncoupling and restart at irreparable UV lesions. Mol. Cell *21*, 15–27.

Lopez-Mosqueda, J., Maas, N.L., Jonsson, Z.O., Defazio-Eli, L.G., Wohlschlegel, J., and Toczyski, D.P. (2010). Damage-induced phosphorylation of Sld3 is important to block late origin firing. Nature *467*, 479–483.

Lossaint, G., Larroque, M., Ribeyre, C., Bec, N., Larroque, C., Décaillet, C., Gari, K., and Constantinou, A. (2013). FANCD2 binds MCM proteins and controls replisome function upon activation of S phase checkpoint signaling. Mol. Cell *51*, 678–690.

Murphy, A.K., Fitzgerald, M., Ro, T., Kim, J.H., Rabinowitsch, A.I., Chowdhury, D., Schildkraut, C.L., and Borowiec, J.A. (2014). Phosphorylated RPA recruits PALB2 to stalled DNA replication forks to facilitate fork recovery. J. Cell Biol. *206*, 493–507.

Neelsen, K.J., and Lopes, M. (2015). Replication fork reversal in eukaryotes: from dead end to dynamic response. Nat. Rev. Mol. Cell Biol. *16*, 207–220.

Petermann, E., Maya-Mendoza, A., Zachos, G., Gillespie, D.A., Jackson, D.A., and Caldecott, K.W. (2006). Chk1 requirement for high global rates of replication fork progression during normal vertebrate S phase. Mol. Cell. Biol. *26*, 3319–3326.

Petermann, E., Woodcock, M., and Helleday, T. (2010). Chk1 promotes replication fork progression by controlling replication initiation. Proc. Natl. Acad. Sci. USA *107*, 16090–16095.

Quinet, A., Lemaçon, D., and Vindigni, A. (2017). Replication fork reversal: players and guardians. Mol. Cell *68*, 830–833.

Räschle, M., Knipscheer, P., Enoiu, M., Angelov, T., Sun, J., Griffith, J.D., Ellenberger, T.E., Schärer, O.D., Walter, J.C., and Walter, J.C. (2008). Mechanism of replication-coupled DNA interstrand crosslink repair. Cell *134*, 969–980.

Ray Chaudhuri, A., Hashimoto, Y., Herrador, R., Neelsen, K.J., Fachinetti, D., Bermejo, R., Cocito, A., Costanzo, V., and Lopes, M. (2012). Topoisomerase I poisoning results in PARP-mediated replication fork reversal. Nat. Struct. Mol. Biol. *19*, 417–423.

Saldivar, J.C., Cortez, D., and Cimprich, K.A. (2017). The essential kinase ATR: ensuring faithful duplication of a challenging genome. Nat. Rev. Mol. Cell Biol. *18*, 622–636.

Schmid, J.A., Berti, M., Walser, F., Raso, M.C., Schmid, F., Krietsch, J., Zwicky, K., Ursich, S., Freire, R., Lopes, M., et al. (2018). Histone ubiquitination by the DNA damage response is Histone ubiquitination by the DNA damage response is required for efficient DNA replication in unperturbed S-phase. Mol. Cell *56*, 92–101.

Schwab, R.A., Blackford, A.N., and Niedzwiedz, W. (2010). ATR activation and replication fork restart are defective in FANCM-deficient cells. EMBO J. *29*, 806–818.

Seiler, J.A., Conti, C., Syed, A., Aladjem, M.I., and Pommier, Y. (2007). The intra-S-phase checkpoint affects both DNA replication initiation and elongation: single-cell and -DNA fiber analyses. Mol. Cell. Biol. *27*, 5806–5818.

Semlow, D.R., Zhang, J., Budzowska, M., Drohat, A.C., and Walter, J.C. (2016). Replication-dependent unhooking of DNA interstrand cross-links by the NEIL3 glycosylase. Cell *167*, 498–511.e14.

Sogo, J.M., Lopes, M., and Foiani, M. (2002). Fork reversal and ssDNA accumulation at stalled replication forks owing to checkpoint defects. Science *297*, 599–602.

Somyajit, K., Basavaraju, S., Scully, R., and Nagaraju, G. (2013). ATM- and ATR-mediated phosphorylation of XRCC3 regulates DNA double-strand break-induced checkpoint activation and repair. Mol. Cell. Biol. *33*, 1830–1844.

Somyajit, K., Gupta, R., Sedlackova, H., Neelsen, K.J., Ochs, F., Rask, M.-B., Choudhary, C., and Lukas, J. (2017). Redox-sensitive alteration of replisome architecture safeguards genome integrity. Science *358*, 797–802.

Thangavel, S., Berti, M., Levikova, M., Pinto, C., Gomathinayagam, S., Vujanovic, M., Zellweger, R., Moore, H., Lee, E.H., Hendrickson, E.A., et al. (2015). DNA2 drives processing and restart of reversed replication forks in human cells. J. Cell Biol. *208*, 545–562.

Thazhathveetil, A.K., Liu, S.T., Indig, F.E., and Seidman, M.M. (2007). Psoralen conjugates for visualization of genomic interstrand cross-links localized by laser photoactivation. Bioconjug. Chem. *18*, 431–437.

Tian, Y., Paramasivam, M., Ghosal, G., Chen, D., Shen, X., Huang, Y., Akhter, S., Legerski, R., Chen, J., Seidman, M.M., et al. (2015). UHRF1 contributes to DNA damage repair as a lesion recognition factor and nuclease scaffold. Cell Rep. *10*, 1957–1966.

Toledo, L.I., Altmeyer, M., Rask, M.-B., Lukas, C., Larsen, D.H., Povlsen, L.K., Bekker-Jensen, S., Mailand, N., Bartek, J., and Lukas, J. (2013). ATR prohibits replication catastrophe by preventing global exhaustion of RPA. Cell *155*, 1088–1103.

Vassin, V.M., Anantha, R.W., Sokolova, E., Kanner, S., and Borowiec, J.A. (2009). Human RPA phosphorylation by ATR stimulates DNA synthesis and prevents ssDNA accumulation during DNA-replication stress. J. Cell Sci. *122*, 4070–4080.

Vujanovic, M., Krietsch, J., Raso, M.C., Terraneo, N., Zellweger, R., Schmid, J.A., Taglialatela, A., Huang, J.-W., Holland, C.L., Zwicky, K., et al. (2017). Replication fork slowing and reversal upon DNA damage require PCNA polyubiquitination and ZRANB3 DNA translocase activity. Mol. Cell *67*, 882–890.e5.

Williams, H.L., Gottesman, M.E., and Gautier, J. (2013). The differences between ICL repair during and outside of S phase. Trends Biochem. Sci. *38*, 386–393.

Yuan, J., Ghosal, G., and Chen, J. (2012). The HARP-like domain-containing protein AH2/ZRANB3 binds to PCNA and participates in cellular response to replication stress. Mol. Cell *47*, 410–421.

Zegerman, P., and Diffley, J.F.X. (2010). Checkpoint-dependent inhibition of DNA replication initiation by Sld3 and Dbf4 phosphorylation. Nature *467*, 474–478.

Zellweger, R., and Lopes, M. (2018). Dynamic architecture of eukaryotic DNA replication forks in vivo, visualized by electron microscopy. Methods Mol. Biol. *1672*, 261–294.

Zellweger, R., Dalcher, D., Mutreja, K., Berti, M., Schmid, J.A., Herrador, R., Vindigni, A., and Lopes, M. (2015). Rad51-mediated replication fork reversal is a global response to genotoxic treatments in human cells. J. Cell Biol. *208*, 563–579.

Zhang, J., and Walter, J.C. (2014). Mechanism and regulation of incisions during DNA interstrand cross-link repair. DNA Repair (Amst.) *19*, 135–142.

Zhang, J., Dewar, J.M., Budzowska, M., Motnenko, A., Cohn, M.A., and Walter, J.C. (2015). DNA interstrand cross-link repair requires replication-fork convergence. Nat. Struct. Mol. Biol. *22*, 242–247.

STAR★METHODS

KEY RESOURCES TABLE

REAGENT or RESOURCE	SOURCE	IDENTIFIER
Antibodies		
anti-DIG antibody	Abcam	Cat# ab76907, RRID:AB_1523496
anti-DIG antibody	Abcam	Cat# ab420, RRID:AB_304362
anti-XPF	Bethyl laboratories	Cat# A301-315A, RRID:AB_938089
anti-MUS81	Sigma-Aldrich	Cat# M1445, RRID:AB_532259
anti-γH2AX antibody	EMD Millipore	Cat# 05-636, RRID: AB_309864
anti-RPA pS4/S8	Bethyl laboratories	Cat# A300-245A, RRID:AB_309864
anti-RAD51	Bio Academia	Cat# 70-002
anti-mouse Alexa 594	Life technologies	Cat# A11032, RRID:AB_141672
anti-rabbit Alexa 488	Life technologies	Cat# A11008, RRID:AB_143165
anti-rabbit Alexa 594	Life technologies	Cat# A11037, RRID:AB_2534095
anti-mouse Alexa 647	Life technologies	Cat# A21235, RRID:AB_141693
anti-mouse Alexa 488	Life technologies	Cat# A10011, RRID: AB_2534069
anti-goat Alexa 647	Life technologies	Cat# A21447, RRID:AB_141844
anti-rat Cy3	Jackson ImmunoResearch	Cat# 712-165-513, RRID: AB_2340669
anti-CHK1pS345	Cell Signaling Techn	Cat# 2348, RRID: AB_331212
anti-CHK1	Santa Cruz	Cat# sc-8408, RRID: AB_627257
anti-Rad51	Santa Cruz	Cat# sc-8349, RRID: AB_2253533
anti-ZRANB3	Bethyl laboratories	Cat# A303-033A, RRID:AB_10773114
anti-FANCM	Prof A. Constantinou lab	N/A
anti-GAPDH	Millipore	Cat# MAB374, RRID: AB_2107445
anti-mouse HRP conjugate	GE Healthcare	Cat# NA931V
anti-rabbit HRP conjugate	GE Healthcare	Cat# NA934V
Rat anti-BrdU/CldU	Abcam	Cat# ab6326, RRID:AB_305426
Mouse anti-BrdU/IdU	BD Biosciences	Cat# 347580, RRID: AB_10015219
Chemicals, Peptides, and Recombinant Proteins		
DIG-TMP	Synthesized for this study	N/A
TMP	Sigma-Aldrich	Cat# T6137
2-Mercaptoethanol	Sigma-Aldrich	Cat# M3148
Lipofectamine RNAiMAX Transfection Reagent	Thermo Fisher Scientific	Cat# 13778-500
cis-Diammineplatinum(II) dichloride	Sigma-Aldrich	Cat# P4934
Protease Inhibitor Cocktail	Sigma-Aldrich	Cat# P8340
ECL Advance Blocking Reagent	GE HealthCare	Cat# RPN418V
Doxycycline hyclate	Sigma-Aldrich	Cat# D9891
5-Chloro-2′-deoxyuridine	Sigma-Aldrich	Cat# C6891
5-Iodo-2′-deoxyuridine	Sigma-Aldrich	Cat# I7125
Proteinase K, recombinant, PCR Grade	Sigma-Adrich	Cat# 03115852001
Blasticidin	InvivoGen	Cat# ant-bl-1
Hygromycin	InvivoGen	Cat# ant-hg-1
Doxycyclin	Sigma-Aldrich	Cat# D9891
Olaparib	Selleckchem	Cat# S1060
AZ20 (ATRi)	Selleckchem	Cat# S7050
VE821 (ATRi)	Selleckchem	Cat# 8007

(*Continued on next page*)

REAGENT or RESOURCE	SOURCE	IDENTIFIER
XL413 (CDC7i)	Selleckchem	Cat# S7547
PvuII high fidelity	New England Biolabs	Cat# R3151S
Critical Commercial Assays		
Click-iT EdU Alexa Fluor 488 Flow Cytometry Assay Kit (FACS)	Thermo Fisher Scientific	Cat# C10425
Click-iT EdU Alexa Fluor 488 Flow Cytometry Assay Kit (Immunofluorescence)	Thermo Fisher Scientific	Cat# C10337
Comet Assay 2 Well ES Unit with Starter Kit	Trevigen	Cat# 4250-050-ESK
Deposited Data		
Raw imaging data	This paper	https://data.mendeley.com/datasets/c2cdh5vfwh/draft?a=56718611-3cfd-4946-9eae-b8f0b4e31994
Experimental Models: Cell Lines		
U2OS	ATCC	HTB-96
ZRANB3 WT U2OS	David Cortez lab	N/A
ZRANB3 KO U2OS	David Cortez lab	N/A
SLX4 Flp-In-TRex U2OS	Pierre-Henri Gaillard lab	N/A
Neil3 WT MEFs	Lusia Luna lab	N/A
Neil3 KO MEFs	Lusia Luna lab	N/A
Oligonucleotides		
siRAD51 F_1: GACUGCCAGGAUAAAGCUUdTdT	Microsynth	N/A
siRAD51 F_2: GUCCUGCAGCCUAAUGAGAdTdT	Microsynth	N/A
siSLX: GCACAAGGGCCCAGAACAAdTdT	Microsynth	N/A
siFANCM: AAGCUCAUAAAGCUCUCGGAAdTdT	Microsynth	N/A
siFANCD2: CAGAGUUUGCUUCACUCUCUAdTdT	Microsynth	N/A
siMUS81: CAGCCCUGGUGGAUGGAUAdTdT	Microsynth	N/A
siXPF: GUAGGAUACUUGUGGUUGAdT dT	Microsynth	N/A
Software and Algorithms		
GraphPad Prism6 and 7 for MAC OS X	GraphPad Software	https://www.graphpad.com/
ImageJ (DNA fiber length analysis, Immunofluorescence, Comet and EM data)	ImageJ Software	https://imagej.nih.gov/ij/
FlowJo (Facs data analysis)	FlowJo Software	https://www.flowjo.com/
Attune Nxt (FACS data acquisition)	Attune NxT Software	https://www.thermofisher.com/
FusionCapt Advance Solo 7 17.02 control and analysis software for chemiluminescence detection (used for western blot)	Vilber Lourmat	http://www.vilber.de/

CONTACT FOR REAGENT AND RESOURCE SHARING

Further information and requests for resources and reagents should be directed to, and will be fulfilled by, the lead contact, Prof. Massimo Lopes (lopes@imcr.uzh.ch).

EXPERIMENTAL MODEL AND SUBJECT DETAILS

Origins of cell lines used in this study are reported in the key resources table.

METHOD DETAILS

Cell Culture and Cell Lines

U20S cells, ZRANB3 proficient and deficient U2OS cells (kind gift from Dr. David Cortez) and SLX4 Flp-In-TRex U2OS cells (kind gift from Dr. Pierre-Henri Gaillard), as well as Neil3 proficient and deficient MEFs (kind gift from Dr. Lusia Luna) were used in this study. All cell lines were cultivated in Dulbecco's Modified Eagle's Medium (DMEM), supplemented with 10% FBS, 100U/mL Penicillin and 10 μg/mL Streptomycin (complete media). Cells were incubated at 37°C in 5% CO^2. For SLX4 cells, 2μg/ml Blasticidin and

200µg/ml Hygromycin were used for selection. For experiments, complete media with Doxycycline (1ng/ml for 24h) but without Blasticidin and Hygromycin was used to allow exogenous SLX4 expression.

Transfections of siRNA Oligos

Cells were transfected with siRNA oligos (40nM) using RNAiMAX (13778500, ThermoFisher) in a Pen-Strep-free media for 12 hours. After that, fresh media containing Pen-Strep and FBS was added to the cells. Cells were collected at different time points after transfection, depending on the protein of interest (see below). The following oligos were used in this study:

RAD51 (24h F_1) - 5′ GAC UGC CAG GAU AAA GCU U dT dT 3′
RAD51 (24h; F_2) - 5′ GUC CUG CAG CCU AAU GAG A dTdT 3′
SLX4 (24h) - 5′ GCA CAA GGG CCC AGA ACA A dT dT 3′
FANCM (48h) - 5′ AAG CUC AUA AAG CUC UCG GAA dT dT 3′
FANCD2 (48h) - 5′ CAG AGU UUG CUU CAC UCU CUA dTdT 3′
XPF (48h) - 5′ GUA GGA UAC UUG UGG UUG A dT dT 3′
MUS81 (48h) – 5′ CAG CCC UGG UGG AUG GAU A dTdT 3′

Drug Treatments

For interstrand-crosslink induction, cells were incubated with DIG-TMP (5 µM, synthesized by the lab of Prof. Dr. Gilles Gasser as described in detail in Methods S1) or TMP (30nM, Sigma) in phenol-free, FBS-free and Pen-Strep-free DMEM media for either 1h or 30 min in the dark. Following this incubation, cells were irradiated with UVA using a UVA chamber (300mJ/cm2 or 3J/cm2) or a UVA laser (laser power at 45%; 50 ms pulses; average nominal power < 10 mW; pulse width < 1 ns; repetition rate > 5 kHz; wavelength 355 nm; typical pulse energy > 0.5 µ J). After irradiation, cells were incubated in complete media and collected at different time points depending on the experiments. Regardless of the type of downstream experimental approach, all manipulation post DIG-TMP/TMP treatment was carried out in the dark.

For experiments involving PARP inhibition, cells were pre-incubated with olaparib (S1060, 10 µM, Selleckchem) for 1hr in in phenol-free, FBS-free and Pen-Strep-free media along with DIG-TMP or TMP. Cells were then irradiated with UVA and incubated in complete media with olaparib. For experiments involving ATR inhibition (AZ20, 1 µM, Selleckchem and VE821, 1 µM, Selleckchem) and CDC7 inhibition (XL413, 10 µM, Selleckchem), ATRi and CDC7i treatment was done in combination with DIG-TMP or TMP in phenol-free, FBS-free and Pen-Strep-free media. Cells were then irradiated with UVA (as above) and incubated in complete media with ATRi or CDC7i or in combination.

DNA Fiber Analysis

Asynchronously growing cells were incubated with DIG-TMP (5 µM) in phenol-free, FBS-free and Pen-Strep-free DMEM media for 1h in the dark. Following this incubation, cells were irradiated with UVA (3J/cm2) and labeled with 30 µM chlorodeoxyuridine (CldU, Sigma-Aldrich), a thymidine analog, for 30min, washed twice with PBS and exposed to 250 µM IdU. The cells were quickly trypsinized and resuspended in PBS at 2.5 × 10⁵ cells per ml. The labeled cells were diluted 1:5 with unlabeled cells, and 2.5 µL of cells were mixed with 7.5 µL of lysis buffer (200 mM Tris-HCl (pH 7.5), 50 mM EDTA, 0.5% (w/v) SDS) on a glass slide. After 9min, the slides were tilted at 15°-45°, and the resulting DNA spreads were air-dried, fixed in 3:1 methanol/acetic acid at 4°C overnight. The next day, slides were denatured using 2.5M HCl for 1h and then washed using PBS. Denatured fibers were then blocked using 1% BSA in PBS. Following the blocking, fibers were incubated with an anti-DIG antibody (Abcam, 1:300) overnight. Next day fibers were washed using 0.2% Tween in PBS (PBST). Fibers were then incubated with an anti-goat antibody Alexa 647 (Life Technologies, 1:1500) for 1h at room temperature in a moisture chamber. Fibers were then washed with PBST and incubated with an antibody against CldU (Abcam, 1:500) and IdU (BD Biosciences, 1:100) for 2.5h in a moisture chamber at room temperature. Fibers were then washed with PBST and incubated with the corresponding secondary antibodies (anti-mouse Alexa488 (Life Technologies, 1:300) and anti-rat Cy3 (Jackson ImmunoResearch, 1:150). After washing 5x3 min in PBST, the slides were air-dried completely, mounted with 60 uL/slide Antifade Gold (Invitrogen). Images were acquired using an Olympus IX81 fluorescence microscope equipped with a CCD camera (Orca AG, Hamamatsu). CldU and IdU tract lengths were measured using ImageJ and the frequency of local replication patterns was determined manually. At least 100 fibers were analyzed per condition. The Kurskal-Wallis test was used to compute the statistical significance in prism (GraphPad Software).

Immunofluorescence

For immunofluorescence experiments cells were grown asynchronously on coverslips or in chamber slides. Pre-extraction was conducted on ice for 5min using Cytoskeletal (CSK) buffer (20mM HEPES pH 7.4, 50mM NaCl, 300mM Sucrose, 3mM MgCl2, EGTA 1mM, Triton X-100 0.5%). After pre-extraction, cells were washed using PBS and fixed for 12 min at RT using 4% Paraformaldehyde. After fixation cells were washed with PBS and permeabilized using 0.3% Triton X-100 in PBS for 10 min at RT. Cells were then incubated with the a primary antibody (see list below) overnight at 4°C. The next day, cells were washed with 0.1% PBST and incubated with the corresponding secondary antibody for 1h at RT in a moisture chamber. Cells were washed with 0.1% PBST and, if indicated in the experiment, EdU click-it Alexa 488 was performed according to the manufacturers protocol (Invitrogen). Cells were then

washed with PBS and stained with DAPI (0.5 μg/ml in PBS). Coverslips/chamber slides were mounted with Prolong gold antifade reagent (Life Technologies). Cells were imaged using a Lecia Microscope (model DMRB) equipped with a camera (model DFC360). ImageJ was used to analyze the images. For EdU intensity measurements a small Region of Interest (ROI) was drawn in the cells away from the ICL signal and the EdU intensity of ROI was measured. For γH2AX intensity measurement of the nucleus, DAPI was used as a mask to mark the nucleus. Kurskal-Wallis test was used to compute statistical analysis in prism (GraphPad Software).

The following antibodies were used:

Anti-DIG (Abcam, #ab420, 1:150), anti-γH2AX (EMD Millipore, #05-636, 1:600), anti-RPA pS4/S8 (Bethyl laboratories, #A300-245A, 1:600), anti-RAD51 (Bio Academia, #70-002, 1:600), anti-mouse 647 (Life technologies, #A31571, 1:500), anti-mouse 594 (Life technologies, #A11032, 1:500), anti-rabbit 488 (Life technologies, #A11008, 1:500) and anti-rabbit Alexa 594 (Life technologies, #A11037, 1:500).

FACS Analysis

For DAPI/EdU/γH2AX analysis by FACS, cells were cells were cultured in the presence of EdU for 30 min prior to trypsinization. Collected cells were spun down at 500 r*cf.*, washed once with PBS and fixed using 4% formaldehyde. After fixation cells were washed using 1%BSA/PBS (blocking buffer). Cells were then incubated in the same blocking buffer on ice for 15 mins. Subsequently, cells were incubated with the primary antibody (anti-γH2AX (EMD Millipore, #05-636, 1:100)) in a 1% saponin buffer (1% saponin in blocking buffer) for 2 h at RT. Next, cells were washed and stained with an anti-mouse A647 secondary antibody (Life Technologies, #A21235, 1:100) for 30 min at room temperature. After a wash with blocking buffer, EdU click-it was performed according to manufacturers protocol (Invitrogen, #C10337). Cells were then washed and incubated with DAPI (1 μg/ml) and RNase A (0.1 μg/ml) for 15 min at room temperature. Cells were analyzed using the Attune Nxt flow cytometer (Life technologies). The FlowJo software was used to determine S-phase cells via gating using the EdU channel and 500 random cells were selected and plotted to measure the intensity of EdU and γH2AX across different samples. The Kurskal-Wallis test was used to compute statistical analysis in prism (GraphPad Software).

Neutral Comet Assay

The Comet assay was performed according to the manufacturers protocol (Trevigen #4250-050- ESK). The Comet assay 2 well ES unit with starter kit was used to perform the assay. The Open Comet plugin of ImageJ was used to analyze the images. At least 50 cells were analyzed and plotted using prism. The Kurskal-Wallis test was used to compute statistical analysis in prism (GraphPad Software).

Western Blotting

Intracellular protein levels were determined by western blot analysis of whole cell extracts as described in the following. Cells were harvested by trypsinization and lysed using 2x laemmili buffer (4% SDS, 20% glycerol, 120 mM Tris-HCl pH6.8). The protein concentration of the whole cell lysates was calculated using the Lowry protein assay. 4%–15% Tris-glycine gels from Biorad were used to carry out electrophoresis. 20 - 30 μg of total protein was loaded per sample and run at 160V for 1.5h. Proteins were transferred to a Nitrocellulose membrane (Immobilon-P membrane, RPN303D, Fisher Scientific) via wet transfer in a buffer containing 20% methanol and 80% 1x transfer buffer (transfer buffer 10x: 25 mM Tris, 192 mM glycine, 10% methanol) using BioRad equipment at 100V for 2hr. After the transfer the membrane was blocked using 2% ECL (GE healthcare #RPN 418) in 0.1% TBST. The blocked membrane was incubated with a primary antibody overnight followed by 3 times 5 min washes with 0.1%TBST. Subsequently, the membrane was incubated with the corresponding secondary antibody for 1 hr at room temperature. Protein bands were detected using ECL detection reagent (Advansta #K12045-D20). The membranes were imaged using Fusion Solo (Vilber smart imaging).

The following antibodies were used:

anti-CHK1pS345 (Cell Signaling Technology, #2348, 1:1000), anti-CHK1 (Santa Cruz Biotechnology Inc., sc-8408, 1:1000), anti-RAD51 (Santa Cruz Biotechnology Inc., #sc-8349, 1:1000), anti- ZRANB3 (Bethyl laboratories, #A303-033A, 1:1000), anti-FANCM (kindly provided by Dr. Angelos Constantinou, 1:500), anti-GAPDH (kindly provided by Dr. Alex Sartori 1:10000), anti-mouse HRP conjugate (GE Healthcare, #NA931V, 1:2500), anti-rabbit HRP conjugate (GE Healthcare, #NA934V, 1:2500).

Electron Microscopy

The procedure was performed as recently described ([Zellweger and Lopes, 2018]), with minor modifications described below. Cells were collected, resuspended in PBS and crosslinked with 4,5′, 8-trimethylpsoralen (10 μg/ml final concentration), followed by irradiation pulses with UV 365nm monochromatic light (UV Stratalinker 1800; Agilent Technologies). For DNA extraction, cells were lysed (1.28M sucrose, 40mM Tris-HCl [pH 7.5], 20mM MgCl2, and 4% Triton X-100; QIAGEN) and digested (800mM guanidine–HCl, 30mM Tris–HCl [pH 8.0], 30mM EDTA [pH 8.0], 5% Tween-20, and 0.5% Triton X-100) at 50°C for 2h in presence of 1mg/ml proteinase K. The DNA was purified using chloroform/isoamylalcohol (24:1) and precipitated in 0.7 volume of isopropanol. Finally, the DNA was washed with 70% EtOH and resuspended in 200 μL TE (Tris-EDTA) buffer. 10U of restriction enzyme (PvuII high fidelity, New England Biolabs) were used to digest 12 μg of mammalian genomic DNA for 4-5 h. Replication intermediates enrichment was performed by QIAGEN Plasmid Mini Kit columns. The QIAGEN-tip 20 surface tension was reduced by applying 1mL QBT buffer. The columns were

washed and equilibrated with 10mM Tris-HCl (pH8.0), 1M NaCl, followed by 10mM Tris-HCl (pH 8.0), 300mM NaCl, respectively. DNA was then loaded onto the columns. The columns were then washed with high NaCl solution (10mM Tris-HCl [pH 8.0] and 850mM NaCl) and eluted in caffeine solution (10mM Tris-HCl [pH8.0], 1M NaCl, and 1.8% [w/v] caffeine). To purify and concentrate the DNA an Amicon size-exclusion column was used. DNA was then resuspended in TE buffer. The Benzyldimethylalkylammonium chloride (BAC) method was used to spread the DNA on the water surface and then load it on carbon-coated 400-mesh copper grids. Subsequently, DNA was coated with platinum using a High Vacuum Evaporator MED 020 (BalTec). Microscopy was performed with a transmission electron microscope (Tecnai G2 Spirit; FEI; LaB6 filament; high tension $\leq$ 120 kV) and picture acquisition with a side mount charge-coupled device camera (2,600 × 4,000 pixels; Orius 1000; Gatan). For each experimental condition at least 70 replication fork molecules were analyzed in two independent experiments (Tables S1–S4). DigitalMicrograph version 1.83.842 (Gatan) and ImageJ (National Institutes of Health) were used to process and analyze the images.

For "immuno-EM" (i.e., ICL labeling with gol-conjugated antibodies), cells were treated with DIG-TMP (5 μM) and UVA (3J/cm^2). DNA was extracted and enriched for replication intermediates as described above. Before spreading the DNA using BAC method, DNA was incubated with a gold labeled anti-DIG antibody, which was custom made by Bio-Synthesis Inc. (Lot no. MB1556-1; size of gold beads 6nm; antibody used for conjugation was anti-DIG from abcam #ab420; 1mg/ml). The conjugated antibody was suspended in a 0.01M sodium phosphate with 0.05% azide, pH 7.2 solution. The antibody (1:100) was incubated with DNA for 1 h at 37°C and then crosslinked with 0.2% glutaraldehyde for 20 min at 37°C. Following the incubation DNA was spread using BAC method with 20% formamide (47671-1L-F Sigma Aldrich).

Chromosomal Breakage and Abnormalities by Metaphase Spreading

Cells were treated for 20 h with 75 nM MMC. The compound was washed off three times with 1x PBS, upon which cells were released into fresh medium containing 200 ng/ml nocodazole for 16 h. Cells were harvested and swollen with 75 mM KCl for 20 min at 37°C. Swollen mitotic cells were collected and fixed with methanol and acetic acid (3:1). The fixing step was repeated two times. Fixed cells were dropped onto pre-hydrated glass slides and air-dried overnight. The following day, slides were mounted with Vectashield medium containing DAPI. Images were acquired with a microscope (model DMRB; Leica) equipped with a camera (model DFC360 FX; Leica) and visible chromatid breaks/ gaps were counted.

Cell Survival by Colony Formation

Cells were seeded onto 60-mm dishes at 60% confluency. Five hours later, cells were treated with TMP, DIG-TMP, MMC and or UVA as indicated. Eight hours after the treatments, 6 × 10^3 cells were seeded in triplicates onto 60-mm dishes and allowed to recover for 7 to 10 days. Resulting colonies were fixed with 100% ice cold methanol and stained with 0.5% Crystal Violet in 100% methanol. Numbers of colonies were counted using a cell counter plug-in for the ImageJ software.

Quantification and Statistical Analysis

For DNA fiber analysis at least 100 tracts were scored per sample. In immunofluorescence and in comet assays, a minimum of 100 and 50 cells were analyzed, respectively. Every experiment was repeated at least twice. To assess statistical significance, the Kurskal-Wallis test was conducted using the GraphPad Prism software (**** = $p < 0.0001$, *** = $p < 0.001$, ** $p < 0.01$, * = $p < 0.05$ and ns = not significant). Every EM experiment was repeated twice and a minimum of 70 molecules were analyzed per sample (Tables S1–S4).

Chemical Synthesis of DIG-TMP

For details on the chemical synthesis of DIG-TMP, see Supplemental Experimental Procedures, Methods S1: "Refined synthesis of DIG-TMP," related to STAR Methods.